TEMPERATURE MEASUREMENTS IN A MULTIPHASE FLUID HAMMER

López Peña, F.* and Lema M.
*Author for correspondence
Department of Marine and Oceanic Engineering,
University of A Coruña,
Rúa da Maestranza, 9
15001 A Coruña, Spain
E-mail: flop@udc.es

Rambaud P. and Buchlin J-M
von Karman Institute for Fluid Dynamics
Chaussée de Waterloo 72, B-1640 Rhode-St-Genèse
Belgium

Steelant J.
Propulsion Design and Aerothermodynamics Section
European Space Agency
Keplerlaan 1, P.O. Box 299, 2200 AG Noordwijk,
The Netherlands

ABSTRACT

Any satellite propulsion system is inactive at launching, having the liquid propellant confined into tanks and the propellant lines vacuum pumped or filled with a non-condensable gas (NCG) at low pressure. Once in orbit, the propulsion system performs the so-called priming maneuver that consists in filling these lines with the pressurized liquid propellant (hydrazine), by opening a fast isolation valve. The opening of this valve subsequently induces a fluid hammer, together with various multiphase phenomena, such as cavitation and gas desorption. On top of that, the adiabatic compression that the liquid propellant may experience can induce the explosive decomposition of hydrazine.

Nowadays, the propulsion systems are certify with CFD simulations, but the numerical models still need to be extended and validated to work with multiphase fluids. The aim of this paper is to study experimentally the pressure and temperature evolution in the propellant lines during water hammer occurrence. The creation of an experimental database is a requirement to validate the numerical tools modeling the propulsion systems.

NOMENCLATURE

C_p	[J/kgK]	Specific heat capacity
m	[kg]	Mass
P_p	[Pa]	Pipe pressure
P_T	[Pa]	Tank pressure
T	[K]	Temperature
u	[m]	Internal energy

INTRODUCTION

The opening of a fast valve commonly generates a fluid hammer that might damage any piping system. This is the case of the propulsion systems in satellites during the priming operation, where the lines are filled with liquid propellant by opening a pyrotechnic valve. Priming has become a major subject of interest on liquid propulsion systems, mainly related to the analysis of the flow transients. One of the first studies found on this subject was presented by Yaggy [1], where he modeled two pipe segments separated by an isolation valve and using real propellants. The author performs a numerical analysis of this configuration, varying the two pipes length, and the initial pressure conditions downstream, concluding that friction played an important role, where the greater unsteady friction factor, compared to the steady value, substantially reduces the pressure surges. Valve opening time was seen to have a minimal effect on peak pressures. Similar conclusions were presented by Prickett et al [2], but using water as test fluid. Furthermore, the use of water produces pressure surges higher than hydrazine and is, therefore, conservative.

The explosive decomposition of hydrazine due to the adiabatic compression during priming was also studied by several authors. Liquid hydrazine is known to undergo exothermic decomposition when the liquid is heated under quasi-static conditions. In 1978 and 1985, Briles [3][4] studied the occurrence of explosive reactions due to the rapid pressure fluctuations taking place in a hydrazine system. It was concluded that the hydrazine detonation threshold is given by the heating process caused by a combination of shock wave phenomena and adiabatic compression, producing hydrazine vapor susceptible of compression ignition

In 1990, Bunker [5] also studied the explosive decomposition of hydrazine by rapid compression of a gas volume. The objective of this study was to determine the initiation mechanism and the explosion mode associated with the hydrazine under rapid compression conditions. According to Bunker, when the hydrodynamic surge pressure was below 17MPa, the resulting pressure appears to be caused only by hydrodynamic effects. When hydrodynamic surge pressure was above 17MPa, the resulting pressure produced by hydrazine is much higher than the hydrodynamic pressure. These results indicate that the hydrazine decomposition occurs at about 17MPa, which corresponds to a critical temperature of 1360K, where the heat loses are minimized and the decomposition reaction accelerates rapidly.

Due to the physical configuration of the system prior to priming, the fluid hammer taking place involves several multiphase phenomena. In particular, the lines are vacuum pumped downstream the pyrotechnic valve, and the propellant is pressurized in the tank with NCG. When the valve opens, the liquid faces a pressure below the vapor pressure, inducing cavitation. In addition, the driving pressure gas at the tanks could be absorbed into the liquid propellant and so it can be desorb during priming, thus increasing the complexity of the process.

An extensive experimental and numerical study on fluid hammer phenomenon in confined environments has been carried out aiming to analyze these priming processes, measuring the pressure and temperature evolution during water hammer occurrence. The goals of this research were twofold; on one hand it aimed to complete the scarce experimental data available in the literature and, on the other, to improve and validate existing numerical models by comparing their results against the experimental data. The main results of this study where focussed on both fluid motion and pressure evolution and have been presented elsewhere [6].

EXPERIMENTAL FACILITY

A new experimental facility has been built including all the elements of a satellite propulsion system directly involved in the fluid hammer occurrence: a pressurized liquid tank, a FOV and a given length of pipe line. The main objective during the design phase was to conceive a facility without singular elements such as elbows and T-junctions upstream of the FOV, and with the same inner diameter in every component. It is well known that these geometrical singularities create secondary pressure waves, which complicate the interpretation of the general pressure measurements. Furthermore, the absence of these elements considerably simplify numerical modeling and result validation when applying CFD codes.

The facility layout is shown in Figure 1, which is intended to be clamped to a vertical wall. The main components are a test vessel, a fast opening valve (FOV) and a given length of the propellant line, referred to as “test element". The line is made with the same titanium tube of 1/4 in. and 0.4 mm thickness, and following the same construction rules used for aerospace applications. Three test element configurations are proposed: straight, 90º elbow and T-bifurcation, but only results with the straight line are considered in this paper. The facility also includes a vacuum system to set the test conditions: test element initially filled with a NCG gas at different pressure levels.

Regarding the FOV, pyrotechnic type valves are avoided in parametric studies and a ball valve with a pneumatic actuator is used instead, resulting in longer opening times, in the vicinity of 40 ms. It is believed that this opening is fast enough to experience a raise in pressure similar to the one obtained with a pyrotechnic valve. This point has been stated by several authors [1] [2] [7] and also verified experimentally in the present study.

The test vessel is a spherical accumulator that mounts an elastic membrane and it is equipped with an ultrasonic transducer to measure the speed of sound in the liquid. The purpose of the membrane is to avoid the absorption of the NCG during the liquid pressurization, allowing to run experiments with deaerated liquid or, when the driving pressure gas is mixed with the liquid, with fully saturated liquid.

The characterization of the pressure front induced by the fluid hammer is achieved through interchangeable measurement modules attached to the bottom end of the test element. The measurement module proposed in this study is instrumented with unsteady pressure and temperature transducers. This facility allows working with inert fluids and nitrogen as driving pressure gas.

TEMPERATURE MEASUREMENTS

Taking into account the difficulties to measure the temperature of a liquid flow under unsteady conditions, the measurements have been limited to record the wall temperature at the impact location. For this purpose, a coaxial thermocouple from the University of Aachen (RWTH) from Germany, shown in figure 2, is flush mounted at the measurement module bottom end. The diameter of the sensing area is 1.9 mm, so the transducer can also be flush mounted next to a pressure transducer on the bottom end (red colored in Figure 3). The RTWH transducers are delivered without any contact between the two metals. In order to create micro junctions between them, the sensing area has to be sanded down with sand paper once it is screwed in the module. That is why the module has to be manufactured with a detachable end plug to have access to the bottom surface.

The wall temperature measurements are not trivial due to all the related heat fluxes taking place on a changing temperature fluid in contact with a solid wall. Generally, the heat transfer between the fluid and the thermocouple is poor, and the heat transfer between the thermocouple and its solid environment by conduction is relatively good, ending with a measured temperature altered by the presence of the thermocouple.

EXPERIMENTAL RESULTS

Test repeatability

With the present facility, the temperature measurement repeatability was found to be poor, as Figure 4 illustrates. Here, the temperature results for three experiments under the same conditions (P_T=2 MPa and P_p=1 kPa), using deaerated water as test fluid, are plotted. The discrepancies among the three results are clear: the temperature raise on the wall goes from 2.3 K in test A, 3.5 K in test C, and up to 5 K in test B. It can also be observed that the temperature evolution before the main peak is not the same for the three test results presented here. In particular, sudden temperature raises in the vicinity of 0.5-1 K appear, and which are different in each experiment. From observations made with a high speed video cámera, it has been deduced that these peaks are due to the impact of liquid pockets preceding the liquid front, and which most probably are a consequence of the liquid flow stratification at the FOV. Figure 5 includes several snapshots recorded with high speed imaging, where liquid pockets and drops of different sizes can be distinguished flowing towards the bottom end before the occurrence of the first pressure peak. In the last snapshot on the right, a mass of liquid has already accumulated at the bottom end before the water hammer takes place. The pressure transducer installed at the same location does not record these phenomenon due to its low sensibility, but the temperature transducer does.

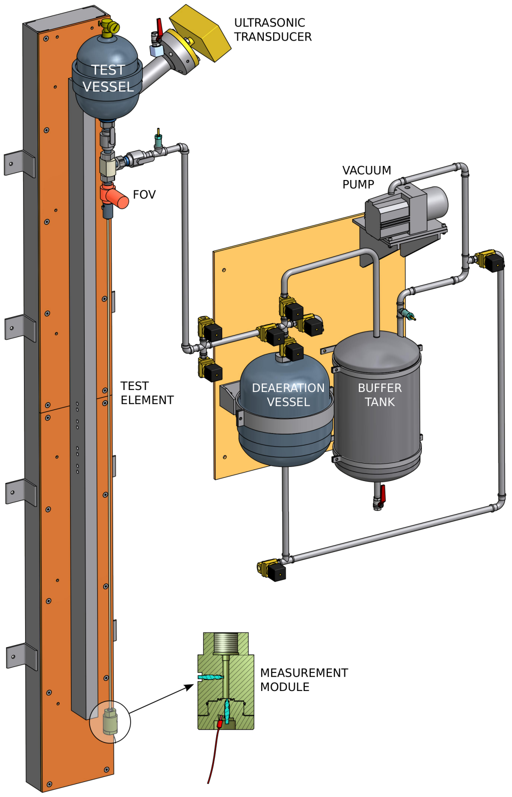

Figure 1 Experimental facility layout. Measurement module attached at the impact location

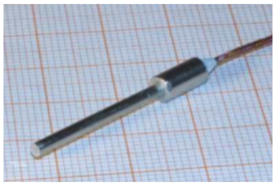

Figure 2 Coaxial thermocouple by RWTH

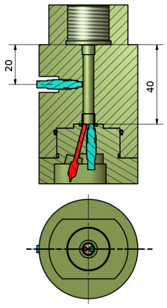

Figure 3 Measurement module with pressure and wall temperature measurements

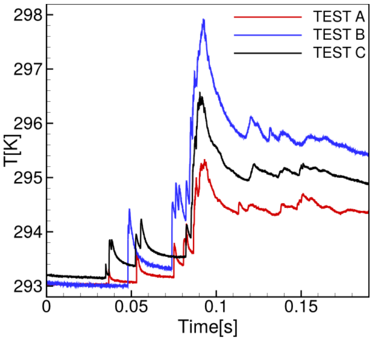

Figure 4 Temperature measurements repeatability

Figure 5 Drops preceding the liquid front arrival

It can be deduced from figure 5 that the number, size and arrival time of liquid pockets reaching the bottom end change from one experiment to another. It can be seen that the arrival of each pocket causes a temperature raise on the wall, and due to the thermal inertia of the material, the initial temperature is not completely recovered before the arrival of the next liquid pocket, inducing a second temperature raise, higher than the previous one. When the liquid front finally arrives, the temperature measured during the water hammer occurrence is affected by the number of previous temperature raises caused by the pockets.

Results analysis

Due to the lack of test repeatability, it has been decided not to carry out a parametric analysis based on the temperature measurements. Instead, a qualitative description of the temperature evolution, combined with the pressure evolution on the bottom end, is performed. Figure 6 presents the pressure and temperature evolution using deaerated water under test conditions P_T=2 MPa and P_p=1 kPa. In this graph, temperature raises coincide with the pressure peaks during water hammer occurrence. The liquid front compression increases the internal energy of the fluid, resulting in the temperature raise observed. The main temperature raise takes place during the first pressure peak, as it could not be otherwise. After this first peak, the temperature signal follows an exponential decay due to the thermal inertia at the wall and heat losses to the ambient, before it grows slightly during the second pressure raise. The third and fourth peaks can be hardly distinguished on the temperature evolution and later, temperature is unaffected by the pressure levels.

On the other hand, figure 7 presents results under the same test conditions, where deaerated ethanol is the working fluid. Now, the maximum temperature raise hardly exceeds 1 K, compared to 5 K obtained with water. Taking into account the specific heat capacity of ethanol, C_p=2460 J/kg K, compared to water, C_p=4180 J/kg K, and the internal energy equation,

$$\Delta u = mC_p\Delta T \tag{1}$$

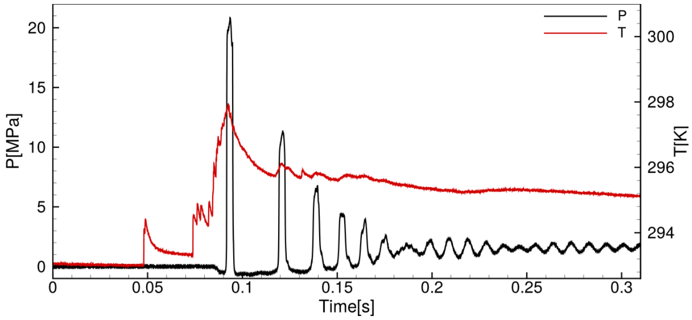

Figure 6 Temperature and pressure measurements. Test conditions: P_T=2 MPa and P_p=1 kPa with deaerated water

the temperature raise with ethanol should not be lower than that with water. On the other hand, the temperature fluctuations with ethanol follow better the pressure peaks, both on the increasing and decreasing side, which is now in agreement with the thermal properties of the liquid. Everything indicates that the absolute values provided by the transducer are not correct, but it still works capturing the temperature fluctuations.

If it is obvious that the temperature measurements have failed to quantitatively capture the water hammer phenomenon, it is less obvious how to provide recommendations for solving the problems found. To install the facility horizontally could reduce the amount of drops on the bottom end, but it would introduce an undesirable asymmetry and, in any case, the liquid front is always preceded by a foamy mixture, which would always affect the measurements.

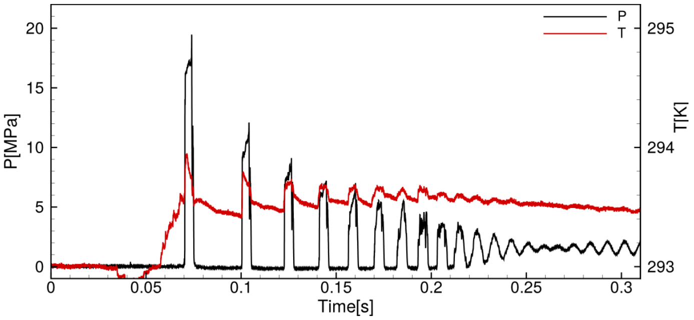

Figure 7 Temperature and pressure measurements. Test conditions: P_T=2 MPa and P_p=1 kPa with deaerated ethanol

CONCLUSION

This paper describes the experiments carried out to study the priming process, with fast response pressure and temperature transducer at the impact location, where the water hammer is originated. For this purpose a coaxial thermocouple from the University of Aachen is flush mounted besides a piezoelectric pressure transducer, both at the bottom end of the pipe line.

The coaxial thermocouple is able to capture the water hammer phenomenon, where the pressure peaks are accompanied by a temperature raise. Unfortunately, the test repeatability appears to be poor, mainly related to the absolute values measured. The liquid patches and foamy mixture preceding the liquid front mightily affect the transducer sensibility, wetting the sensing area and, thus, changing the heat transfer coefficient of the material. Placing the facility horizontally could help to improve the temperature measurements, at the cost of adding singular element to the flow path, such as elbows and T-junctions, as well as a force perpendicular to the flow path that could introduce undesirable asymmetries.

AKNOWLEDGEMENT

The present research activity was initiated and promoted by the European Space Research and Technology Centre of the European Space Agency (ESTEC/ESA). It has been also founded by the Xunta de Galicia and European Regional Development Funds under grant GRC 2013-050.

REFERENCES

[1] K. L. Yaggy. Analysis of propellant flow into evacuated and pressurized lines. In 20th AIAA/SAE/ASME Joint Propulsion Conference and Exhibit, 1984.

[2] R. P. Prickett, E. Mayer, and J. Hermal. Water hammer in a spacecraft propellant feed system. Journal of Propulsion and Power, 8(3):592–597, 1992.

[3] Briles, O. M. and Hollenbaugh, R. P. Adiabatic compression testing of hydrazine. In AIAA/SAE 14th Joint Propulsion Conference, Las Vegas, USA, 1978.

[4] Briles, O., Hagemann, D., Benz, F., and Farkas, T. Explosive decomposition of hydrazine due to rapid gas compression. Technical report, White Sands Test Facility, 1985.

[5] Bunker, R. L., Baker, D. L., and Lee, J. H. S. Explosive decomposition of hydrazine by rapid compression of a gas volume. Technical report, Johnson Space Center, White Sands Test Facility, 1990.

[6] M. Lema, F. Lopez Peña, J-M. Buchlin, P. Rambaud, J. Steelant, “Fluid hammer with gas desorption in a liquid filling pipe system” (Submitted to “Experiments in Fluids”).

[7] T. Y. Lin and D. Baker. Analysis and testing of propellant feed system priming process. Journal of Propulsion and Power, 11(3):505–512, 1995.

A SIMULTANEOUS APPLICATION OF PLIF-PIV-PTV FOR THE DETAILED EXPERIMENTAL STUDY OF THE HYSRODYNAMIC CHARACTERISTICS OF THIN FILM FLOWS

Charogiannis A.[1], Denner F.[2], Pradas M.[1], Kalliadasis S.[1] van Wachem B.G.M.[2] and Markides C.N.[1]*
*Author for correspondence
Department of Chemical Engineering[1], Department of Mechanical Engineering[2]
Imperial College London, London, SW7 2AZ, United Kingdom,
E-mail: c.markides@imperial.ac.uk

ABSTRACT

Films falling over flat inclined plates are employed over a broad range of industrial applications owing to their superior heat and mass transfer capabilities. However, and despite extensive research efforts, many aspects of the dynamics of the particular class of interfacial flows still elude us. This paper reports on the application of Laser-Induced Fluorescence imaging alongside simultaneous Particle Image/Tracking Velocimetry to isothermal, harmonically excited, gravity-driven liquid films, in order to spatiotemporally resolve the flow field underneath the wavy interface. Results generated using this experimental methodology are expanded to provide information on spatiotemporally resolved mass transfer characteristics and pursue comparisons to analytically derived estimates. The latter are observed to severely overestimate the experiments depending on flow conditions and wave topology. Finally, the effect of unsteadiness is brought into focus by decomposing the time-varying flow rate into mean and fluctuating components. The latter is shown to vary linearly with the variance of the film thickness for each of the two liquids presently examined.

INTRODUCTION

The present paper is dedicated to an experimental investigation of isothermal, harmonically excited, gravity-driven liquid films flowing over a flat inclined plate. Owing to their high surface-to-volume ratios and superior heat and mass transfer capabilities, such films are employed in a broad range of industrial applications, including wetted-wall absorbers, condensers, evaporators and reactors. It comes as no surprise, therefore, that extensive theoretical [1], experimental [2] and numerical [3] efforts have been devoted to relevant studies since the first systematic work was published by Kapitza and Kapitza [4].

Despite the extensive body of previous experimental work, only a limited number of publications relating to simultaneous spatiotemporal variations of the film thickness and velocity in the flows of interest is available; an observation inherently linked to the restricted liquid domain under observation and the intermittent nature of the moving and wavy interface that makes such measurements particularly challenging. Nevertheless, recent efforts utilizing advanced optical techniques such as Chromatic Confocal Imaging (CCI), Laser-Induced Fluorescence (LIF), Particle Image/Tracking Velocimetry (PIV/PTV) and micro-PIV have enhanced our understanding of the underlying complex flow phenomena. For example, Dietze and co-workers [5, 6] (using CCI and micro-PIV) were the first to experimentally observe backflow in the capillary wave regions, Adomeit and Renz [7] (using micro-PIV) noted deviations from Nusselt velocity profile predictions depending on film topology, and Zadrazil and Markides [8, 9] (using LIF and PIV) observed multiple recirculation zones within disturbance waves in downwards annular flows.

Despite such novel insights, a comprehensive study linking spatiotemporally resolved flow field measurements to the mass transfer characteristics of films flows is still lacking; the present paper, therefore, aims to fulfil this requirement. In greater detail, the paper reports on an application of LIF imaging alongside simultaneous PIV and PTV to falling, planar thin-film flows in order to spatiotemporally resolve the flow field underneath the wavy interface. The results from this approach, whose original development was reported in Ref. [11] and which is extended here to provide information on spatiotemporally resolved mass transfer characteristics, can offer powerful insights into the hydrodynamics of the particular class of interfacial flows, while generating useful validation data for advanced modelling efforts.

NOMENCLATURE

D	[m]	Characteristic dimension for the *Re* number definition
f	$[s^{-1}]$	Forcing/wave frequency
g	$[m/s^2]$	Gravitational acceleration
Ka	[-]	Kapitza number
Q	$[m^3/s]$	Steady flow rate
Q'	$[m^3/s]$	Unsteady flow rate
Re	[-]	Reynolds number
t	[s]	Time
v	$[m^2/s]$	Kinematic viscosity
w	[m]	Film span
x	[m]	Distance along the film
y	[m]	Distance from the wall

Special characters

β	[°]	Film inclination angle
Γ	$[m^2/s]$	Flow rate per unit width of the flow
δ	[m]	Film thickness
ρ	$[kg/m^3]$	Density
σ	[N/m]	Surface tension

Subscripts

b	Bulk: Referring to velocity
box	Flow distribution box
f	Fluid
N	Nusselt: Referring to the Nusselt solution
std	Standard deviation

Overall, the experimental campaign comprises four different Kapitza (*Ka*) number liquids (aqueous glycerol solutions), Reynolds (*Re*) numbers spanning the 2 - 320 range, and inlet forcing frequencies between 1 and 10 Hz. In this contribution, presented results will be limited to select conditions, mainly focusing on the effect of unsteadiness on the mass transport characteristics of the examined films, as well as on comparisons with analytical calculations. The definitions of two primary experimental parameters, namely the *Re* and *Ka* numbers are given in Equations (1) and (2). *Ka* represents the dimensionless ratio of surface tension to inertial forces, and stands for an indicator of the hydrodynamic wave regime.

$$Re = \frac{DU}{\nu_{\mathrm{f}}} \tag{1}$$

$$Ka = \frac{\sigma_{\mathrm{f}}}{\rho_{\mathrm{f}} \nu_{\mathrm{f}}^{4/3} \left(g \sin\beta\right)^{1/2}} \tag{2}$$

EXPERIMENTAL SETUP

A detailed description of the experimental setup can be found elsewhere [10], yet a synopsis is provided here for completion. The liquid circulates within a closed loop comprising a 0.7 mm thick, 400×285 mm soda lime glass plate over which the desired film flows develop (Figure 1).

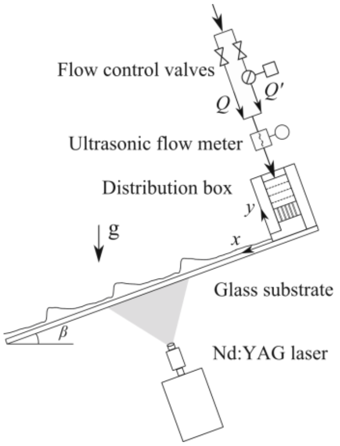

Figure 1 Schematic of the experimental test section.

The plate itself is mounted on an aluminium frame inclined at $\beta = 20°$ to the horizontal, while a distribution box has been installed in order to uniformly dispense the flow over the plate and minimise turbulence at the inlet. The box outlet has been equipped with a knife-edge, the height of which is adjusted to regulate the flow contraction and prevent the generation of a hydraulic jump or any backflow. Using the mean flow rate measurement from an ultrasonic flowmeter installed at the box supply, a *Re* number can be defined as in Equation (3), where U_{box} stands for the velocity, D for the channel depth (20 mm) and Γ for the flow rate per unit width of the channel (285 mm).

$$Re = \frac{DU_{\mathrm{box}}}{\nu_{\mathrm{f}}} = \frac{\Gamma}{\nu_{\mathrm{f}}} \tag{3}$$

Upstream of the distribution box, the flow is split into a steady (Q) and a pulsating supply (Q'), the latter generated using a rotating valve, allowing for accurate control of both wave frequency and amplitude. In this way, fully developed wave regimes were obtained within the confines of a short test section. Excitation of the dye and particle seeded flow was performed from the wall side (i.e., from underneath) using a double-cavity frequency-doubled Nd:YAG laser (100 Hz). This avoided illuminating the liquid from the wavy interface, which would have subjected the laser sheet (approximately 200 μm thick) to strong, spatially and temporally non-uniform distortions and lensing. Imaging was also carried out from below so as to limit image distortions. The imaging setup comprises a pair of LaVision VC-Imager Pro HS 500 CMOS cameras equipped with Sigma 105 mm f/2.8 Macro lenses and extension rings (32 mm) in order to achieve the desired magnification. Both cameras and lasers were synchronized by a LaVision High Speed Controller (HSC) and operated using the LaVision Davis 8.2.1 software.

Variations to the *Ka* number, which constitutes one of our primary objectives, can be imposed by tailoring the liquid viscosity and density; therefore the implementation of a novel refractive index correction tactic was necessary [11]. In particular, the imaging planes of both cameras were mapped and corrected for perspective distortions using a calibration graticule immersed inside the employed liquid solution, and a pinhole model available in Davis. To this end, a Perspex box with its bottom surface removed (the one that would otherwise adhere to the glass) was carefully positioned at the excitation plane using a micrometer stage and subsequently filled with the liquid. The apparent resolution for the presently examined *Ka* numbers was between 28.0 and 29.7 μm/pixel, with the fit root mean square (RMS) errors ranging between 0.5 and 0.9 pixels and the imaging domain along the film extending to approximately 33 mm. A short-pass filter with a cut-off frequency at 550 nm was installed on the PIV camera, while a long-pass filter with a 540 nm cut-off frequency was used for LIF. The dye (Rhodamine B) concentration was approximately 0.5 g/L, while glass hollow spheres (11.7 μm mean diameter) were seeded at a concentration of approximately 0.18 g/L for tracking the fluid motion.

EXPERIMENTAL METHOD

Both cameras were operated in dual-frame mode, so that for every PIV frame a corresponding LIF frame was acquired. The interframe separation was varied between 0.45 and 1.50 ms, allowing for particle displacements of 8 – 15 pixels at the interface. A sample perspective distortion corrected LIF frame along with its processed counterpart are presented in Figure 2. Close inspection of raw LIF images reveals that the fluorescence emitted by the film is reflected about the gas-liquid interface, while reflections by the glass substrate blur the LIF signal locally. The location of the solid-liquid interface was obtained directly from the LIF images using an edge detection algorithm [12], while with respect to the gas-liquid interface, intercepts between linear fits to maximum signal gradients and reflection intensity profiles were employed as estimates of the liquid boundary. Compared to alternative tactics that were considered, based on a threshold intensity and a maximum gradient intercept with the zero intensity axis approaches, the selected method produced smoother results and was more robust in regions with locally stronger reflections.

(a) Raw LIF Image

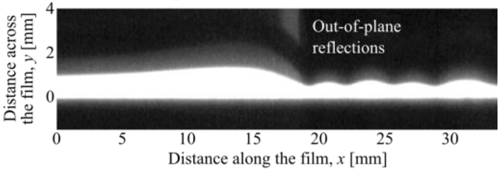

(b) Processed LIF Image

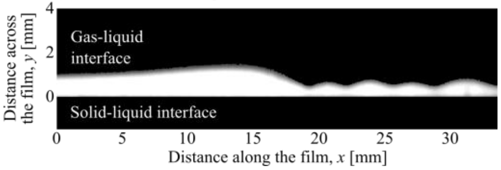

Figure 2 (a) Refractive index and perspective distortion corrected LIF image, and (b) corresponding fully processed LIF image, for a film flow with Re = 129.4, Ka = 1799, f_w = 10 Hz.

(a) Raw Particle Image

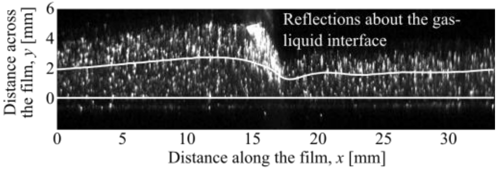

(b) Masked Particle Image

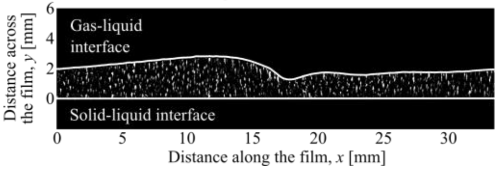

Figure 3 (a) Refractive index and perspective distortion corrected particle image, and (b) corresponding fully processed image, for a film flow with Re = 26.93, Ka = 84.87, f_w =10 Hz.

Similarly to the LIF images, reflections of primary scattered signals from to the entire illuminated liquid volume appeared above the gas-liquid interface in the raw PIV images (Figure 3 (a)). In this case, however, the reflection intensities were comparable to the original signals, rendering the identification of secondary scattering sources as such, highly non-trivial. Thus, binarized LIF images were imported in Davis and used to mask out any regions associated with out-of plane reflections. The masked particle images were then used to generate two-dimensional velocity vector maps by means of a four-pass cross-correlation approach. For the first and second passes, a 32×32 pixel interrogation window was selected with a 50% overlap. For the third and fourth passes, the interrogation window was reduced to 16×16 pixels. The resulting vector-to-vector PIV spatial resolution is estimated as being between 222.4 and 236.6 μm, depending on the experimental round. Finally, individual particles were tracked (PTV calculation) by employment of the obtained PIV results as reference estimators of the velocity field. A comprehensive account of all processing steps employed in the LIF, PIV and PTV vector field calculations can be found in Ref. [13]. PTV, rather than PIV was favoured in the present study due to the superior spatial resolution on offer, as well as the reduced propensity towards bias errors in the presence of gradients [14].

In order to examine the velocity distributions underneath the waves in detail, the practice of phase-averaging PTV maps corresponding to the same spatial domain was adopted. The primary challenge was to identify which images could be averaged out and by how much each would need to translated in the axial direction so as to match the desired topology. A film thickness profile (reference signal) pertaining to the desired topology was initially selected and cross-correlated with all available thickness traces from the same data set. Signal pairs satisfying a maximum displacement condition (80 pixels) where repositioned and averaged, as where the corresponding PTV images (Figure 4).

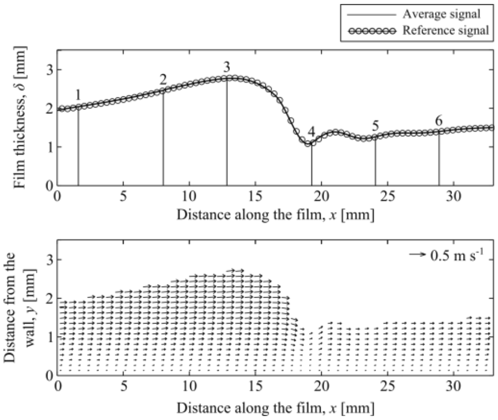

Figure 4 (Top) Phase-averaged wave profile (and reference wave-locations; see Figure 5) for a liquid-film flow with Re = 26.93, Ka = 84.87 and f_w = 10 Hz. (Bottom) Corresponding average liquid-phase PTV velocity field for the same flow.

A series of experiments were conducted in order to assess the validity of the combined optical methodology. First, film thicknesses from flat (unforced) films (Ka = 14.06) were compared to micrometer stage measurements, as well as the one-dimensional, steady, fully developed solution of the Navier-Stokes equation under the assumption of negligible inertia, also known as the Nusselt solution [15]. The resulting deviations were around 20 μm for both tests; less than the apparent image resolution. Relative deviations were calculated between PTV derived interfacial and bulk velocities and analytical results, with mean values amounting to 3.2% for both test cases, while flow rate comparisons were conducted between LIF/PTV derived and flowmeter data. The mean relative deviation was 1.6% for a total of six flat and nine wavy flows. The Nusselt expressions for the film thickness δ_N, and bulk velocity U_{Nb}, are given below (these will be employed later on in comparisons with optical measurement results).

$$\delta_N = \left(\frac{3\nu_f Q}{gw \sin\beta} \right)^{1/3} \tag{4}$$

$$U_{Nb} = \frac{g \sin\beta \delta_N^{\ 2}}{3\nu_f} \tag{5}$$

TRENDS AND RESULTS

Velocity Profiles

By implementing the previously described experimental methodologies and processing steps, the flow field underneath the wavy liquid-air interface can be examined for a broad range of harmonically excited films, including direct comparisons to analytical calculations. A similar analysis attempted by other researchers [7, 16], though to our knowledge only for unforced film flows, concentrated on axial velocity profile comparisons to analytically derived ones. Effectively, results from the Nusselt solution are compared to experimentally derived ones for the flow field behind, underneath, and ahead of the wave crest. It is noted that these calculations are based on the experimentally derived film thickness data. By inspection of the results in Figure 5 (corresponding to the numbered locations along the wave in Figure 4), it is evident that the analytical prediction nearly matches the experiment behind the wave crest, significantly overestimates it in close vicinity to the wave crest, and slightly underestimates it in the capillary wave zone, in agreement with earlier observations in Refs. [7, 16]. In more detail, the absolute deviations between the experimentally derived and calculated interfacial velocities amount to less than 10% at Location 1, around 35% at Location 2, 70% at Location 3, nearly 15% at Location 4, and approximately 25% at Locations 5 and 6. Both the trend and deviation magnitudes agree well with results published in Ref. [16] for a *Re* = 16 and *Ka* = 18.54 laminar film falling down a 45° inclined plate.

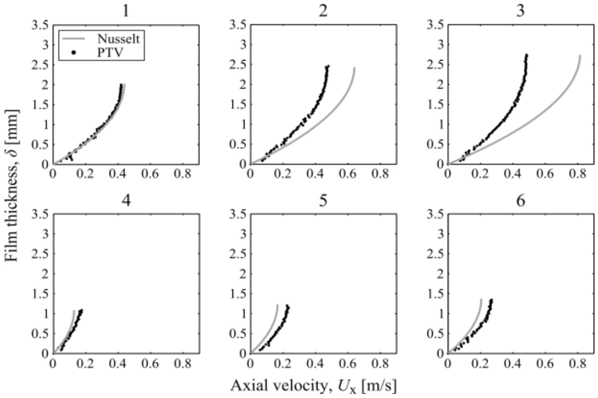

Figure 5 Experimental (PTV) and analytically derived (Nusselt solution) axial velocity profiles corresponding to the six numbered wave-locations indicated in Figure 4 (top).

Flow Rates

The preceding analysis was then expanded to allow for flow rate comparisons between waves from different flows, as well as their analytically derived counterparts. In more detail, each axial velocity profile along an averaged PTV map, such as the one previewed in Figure 4, was integrated using the trapezoidal rule and multiplied by the local film thickness and film span. For the same film height values, bulk velocities were calculated using the corresponding Nusselt relationship yielding flow rate predictions. Sample results are shown in Figure 6.

Despite the fact that different *Ka* and *Re* flows were selected for the particular comparative assessment, the mean flow rates for all three flows are nearly identical (within 5%). For the *Ka* = 14.06 flow, deviations between experiments and analytically calculated results are small, with the mass carrying capacity of the wave being slightly lower than the analytical results suggest, and the flow rate ahead of the wave being slightly underestimated. As the *Ka* number increases the aforementioned trend persists; however, the deviation near the wave crest increases to nearly 65%. For the *Ka* = 346.2 flow, the calculated flow rate at wave the crest exceeds the experimental value by more than 100%.

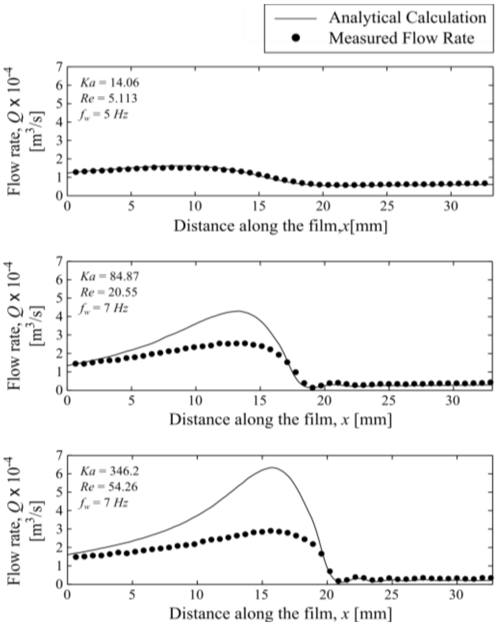

Figure 6 Flow rate comparisons between experiments and analytical calculations for waves in flows with *Ka* = 14.06 (top), *Ka* = 84.87 (middle), and *Ka* = 346.2 (bottom) liquids.

An equivalent analysis was pursued for time-varying flow rate results generated using the following approach: film thickness data were averaged along a 1.8 mm region of the flow on a per image basis, while averaged axial velocity profiles were generated over the same spatial domain and subsequently integrated over the liquid domain. Thus, every LIF/PTV image pair contributed a single, local and instantaneous flow rate measurement; upon averaging all individual flow rates over an entire data set corresponding to a fixed flow condition, a mean flow rate can be obtained and compared to the flow meter measurement for validation purposes. The latter were found to deviate by only 2.1% on average over 50 studied flow comparisons.

Flow rate time traces (over one second) are presented in Figure 7 for flows with *Ka* = 84.87 and *Re* = 10.64, 14.29, 20.55 and 24.72, alongside complementary analytical results. The latter once again stem from bulk velocity estimates generated using experimentally derived local film thickness data. As the *Re* number increases, this time by increasing the flow rate, the deviations between experiments and analytical results grow in a similar fashion to the one observed earlier; films characterized by stronger flow rate fluctuations display higher deviations. Also in agreement with the previous assessment, absolute deviations peak in close vicinity to the wave crests. It is therefore evident from the so-far presented results that the examined analytical approach fails to reproduce the experimentally obtained data, as the velocities underneath the waves fall significantly short of the values expected from theoretical analyses relying on the Nusselt solution.

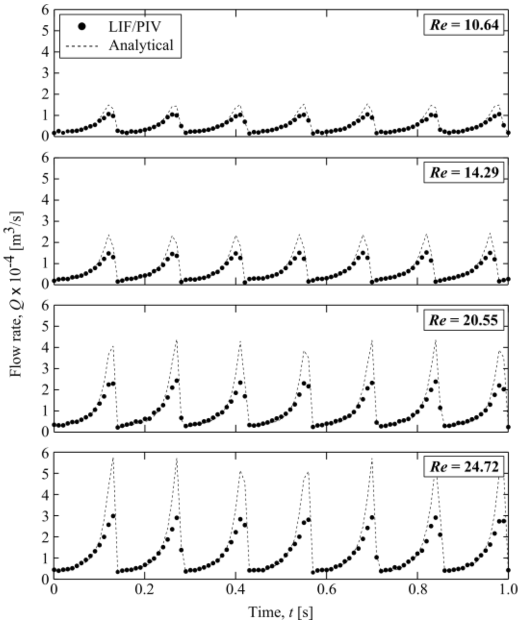

Figure 7 Flow rate time traces over 1 s obtained from simultaneously conducted LIF and PTV measurements, and presented along with complementary analytical results.

Mass transfer characterization

The impact of unsteadiness on the mass carrying capacity of harmonically excited film flows can be examined more rigorously by a Reynolds decomposition of the time-varying flow rate into mean and fluctuating components:

$$Q = \overline{Q} + Q' \tag{6}$$

Equation (6) can be normalized by the span (which is constant) and expanded into a function that includes the mean and fluctuations of the bulk velocity and film thickness:

$$\overline{Q} = \overline{U_{\mathrm{b}}}\,\overline{\delta} + \overline{U_{\mathrm{b}}'\delta'} \tag{7}$$

The first term in Equation (7), hereby referred to as the "steady term", is the product of the time-averaged bulk velocity and film thickness, and corresponds to the flow rate of an equivalent *steady* film flow (without waves) that has a bulk velocity and thickness equal to the averaged bulk velocity and thickness of the actual flow under investigation. The second term, designated the "unsteady term", is the covariance (time-averaged product) of the two fluctuating terms, and represents the coupling between the local and instantaneous film thickness and velocity. For a flat film (where the flow rate is constant) the unsteady term is equal to zero and the mean bulk velocity calculation is straightforward. The introduction of waviness (Figure 8) entails a non-zero unsteady term and a consequent deviation between the analytical calculation and experiment; the time-averaged U_{b} is overestimated due to significant velocity deviations underneath the waves, which grow with increasing unsteadiness (stronger flow rate fluctuations).

In consequence of these observations, an alternative approach to the experimental-analytical comparative studies so far conducted has been pursued and is hereby presented. Going back to the flow rate breakdown of Equation 7, the LIF and PTV results allow us to calculate time-averaged flow rates (Q), as well as time-averaged U_{b} and δ values; unsteady terms can then be obtained directly from Equation 7. For the same experimentally derived time-varying flow rate trace, film thicknesses and bulk velocities can be calculated at each measurement point using the Nusselt expressions. If processed in the same manner as the experimental results, steady and unsteady terms can be generated. This approach was implemented over a total of 46 flows, 21 originating from the *Ka* = 346.2 data set, and 26 from the *Ka* = 84.87 data set. Based on the results of this analysis, shown in Figures 8 and 9, the following remarks can be made:

1. Analytical predictions consistently match the experimentally retrieved steady terms, with a mean absolute deviation of 0.77%. This is evidenced by the corresponding data point overlap in Figure 8.
2. The steady term scales linearly with *Re* for each of the two *Ka* data sets; a relatively unsurprising outcome given that both mean bulk velocity and thickness are included in the film *Re* definition.
3. For the *Ka* = 84.87 flows, the ratio of unsteady to steady terms increases with increasing *Re* and then falls off at around *Re* = 20, spanning the range 2.2% - 12.44%.
4. Regarding the *Ka* = 346.2 data, increasing the *Re* consistently results in a reduction in the relative magnitudes of the unsteady terms. The latter are, however, considerably higher compared to the *Ka* = 84.87 flows, ranging from 7.8% to 25%.
5. An inverse trend is observed between the ratio of unsteady to steady terms and the wave frequency; from 5 to 7 and then to 10 Hz, relative unsteady terms diminish (*Ka* = 84.8). The same trend is observed for the *Ka* = 346.2 flows (only 7 Hz and 10 Hz cases were examined for the particular liquid solution).
6. The mean deviation between experimentally obtained and analytically derived unsteady terms, over all examined flow conditions, is 7.5%. It may be speculated that this deviation is linked to the one noted earlier regarding the steady terms, although this requires further work to ascertain.
7. Finally, for both *Ka* number liquids, the unsteady term scales linearly with the variance of the film thickness, effectively a measure of film waviness (Figure 9).

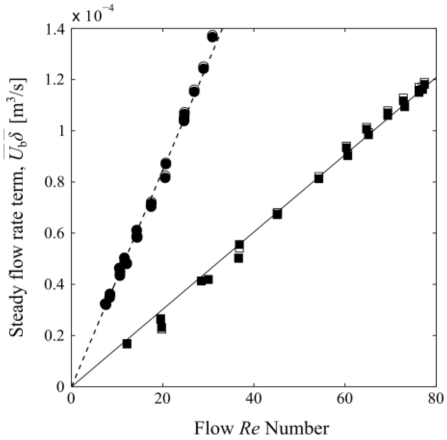

Figure 8 Steady flow rate terms for flows with *Ka* = 84.87 and *Ka* = 346.2 as a function of the flow *Re*. For legend see Figure 9.

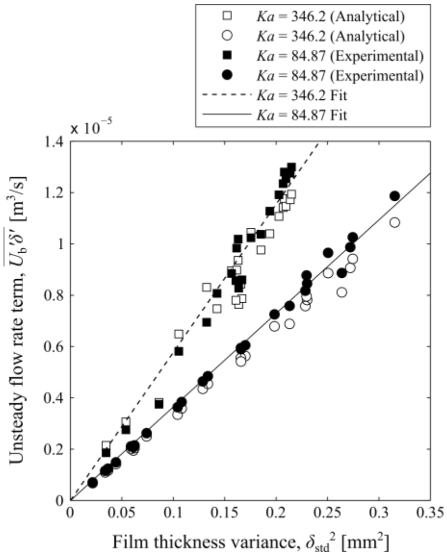

Figure 9 Unsteady flow rate terms for flows with Ka = 84.87 and Ka = 346.2 against corresponding film thickness variances.

CONCLUSION

The deviations observed in flow rate comparisons between waves from different flows and their analytically derived counterparts are linked to the wave topology. With increasing *Ka* and *Re* numbers, the wave mass carrying capacity is increasingly overestimated by the analytical calculation, with deviations exceeding 100% near the wave crest. In contrast, analytically calculated velocity profiles behind the crest agree well with experiments, while ahead of the wave crest, the latter typically exhibit lower velocities than the experimentally observed ones. Along with the comparative analysis carried out for phase-averaged wave profiles, time-varying flow rate comparisons were pursued, with the results suggesting that films characterized by stronger flow rate fluctuations display consistently higher deviations. Also in agreement with the previous assessment, absolute deviations peak in close vicinity to the wave crests.

As the examined analytical approach failed to reproduce the experimentally obtained data, the impact of unsteadiness on the mass carrying capacity of harmonically excited films was examined by a Reynolds decomposition of the time-varying flow rate into mean and fluctuating components. In that case, analytical predictions consistently matched the steady terms (product of the time-averaged bulk velocity and thickness), which scaled linearly with the *Re* number. Close agreement (mean deviation of 7.5%) was also observed between experimentally and analytically derived unsteady terms (covariance of the fluctuating thickness and bulk velocity), which were found to scale linearly with the film thickness variance, effectively a measure of film waviness.

ACKNOWLEDGEMENTS

This work was supported by the Engineering and Physical Sciences Research Council (EPSRC), UK [grant number EP/K008595/1].

REFERENCES

[1] Pradas, M., Tseluiko, D. and Kalliadasis, S., Rigorous coherent-structure theory for falling liquid films: Viscous dispersion effects on bound-state formation and self-organization, *Phys. Fluids*, Vol. 23, 2011, pp. 044104-1-19

[2] Mathie, R., Nakamura, H. and Markides, C. N., Heat transfer augmentation in unsteady conjugate thermal systems - Part II: Applications, *Int. J. Heat Mass Transfer*, Vol. 56, 2013, pp. 819-833

[3] Rohlfs, W. and Scheid, B., Phase diagram for the onset of circulating waves and flow reversal in inclined falling films, *J. Fluid Mech.*, Vol. 763, pp. 322-352

[4] Kapitza, P. L., Wave flow of thin layers of a viscous fluid: I. Free flow, *Zhurnal Eksperimentalnoi I Teoreticheskoi Fiziki*, Vol. 18, 1948, pp. 3-18

[5] Dietze, G. F., Al-Sibai, F. and Kneer, R., Experimental study of flow separation in laminar falling liquid films, *J. Fluid Mech.*, Vol. 637, 2009, pp. 73-104

[6] Dietze, G. F., Leefken, A. and Kneer, R., Investigation of the backflow phenomenon in falling liquid films, *J. Fluid Mech.*, Vol. 595, 2008, pp. 435-459

[7] Adomeit, P. and Renz, U., Hydrodynamics of three-dimensional waves in laminar falling films, *Int. J. Multiphase Flow*, Vol. 26, 2000, pp. 1183-1208

[8] Zadrazil, I., Matar, O. K. and Markides, C. N., An experimental characterization of downwards gas-liquid annular flow by laser-induced fluorescence: Flow regimes and film statistics, *Int. J. Multiphase Flow*, Vol. 60, 2014, pp. 87-102

[9] Zadrazil, I., Matar, O. K. and Markides, C. N., An experimental characterization of liquid films in downwards co-current gas-liquid annular flow by particle image and tracking velocimetry, *Int. J. Multiphase Flow*, Vol. 68, 2014, pp. 1-12

[10] Charogiannis, A. and Markides, C. N., Experimental Study of Falling Films by Simultaneous Laser-Induced Fluorescence, Particle Image Velocimetry and Particle Tracking Velocimetry, *17th International Symposium on Applications of Laser Techniques to Fluid Mechanics, Lisbon, Portugal*, 2014

[11] Budwig, R., Refractive index matching methods for liquid flow investigations, *Exp. Fluids*, Vol. 17, 1994, pp. 350-355

[12] Zhu, Y. M., Kaftandjian, V., Peix, G. and Babot, D., Modulation transfer function evaluation of linear solid-state x-ray-sensitive detectors using edge techniques, *Appl. Opt.*, Vol. 34, 1995, pp. 4937-4943

[13] Charogiannis, A., An, J. S. and Markides, C. N., A Simultaneous Laser-Induced Fluorescence, Particle Image Velocimetry and Particle Tracking Velocimetry Technique for the Investigation of Liquid Film Flows, *Exp. Therm. Fluid Sci.*, *submitted, in peer review*

[14] Kähler, C. J., Scharnowski, S. and Cierpka, C., On the uncertainty of digital PIV and PTV near walls, *Exp. Fluids*, Vol. 52, 2012, pp. 1641-1656

[15] Nusselt, W., Die Oberflachenkondensation des Wasserdampfes, *Z. Vereines Deutscher Ingenieure*, Vol. 60, 1916, pp. 541-546

[16] Moran, K., Inumaru, J. and Kawaji, M., Instantaneous hydrodynamics of a laminar wavy liquid film, *Int. J. Multiphase Flow*, Vol. 28, 2002, pp. 731-755

APPLICATION OF SUBGRID STRESS MODEL TO VOLUMETRIC PIV RESULTS FOR ESTIMATION OF TURBULENCE DISSIPATION RATE IN A STIRRED MIXER

Shekhar C.*[1], Takahashi K.[2], Matsunaga T.[3] and Nishino K.[2]

[1]Heat and Fluid Dynamics Laboratory, IHI Corporation, Yokohama, Japan
[2]Department of Mechanical Engineering, Yokohama National University, Japan
[3]Department of Systems Innovation, The University of Tokyo, Tokyo, Japan

*Author for correspondence
Heat and Fluid Dynamics Laboratory, IHI Corporation,
1, Shin-Nakahara-Cho, Isogo-ku, Yokohama 2358501, Japan,
E-mail: chandraiitk@yahoo.co.in

ABSTRACT

We analyzed applicability of subgrid-stress model to volumetric (tomographic) PIV results, in order to estimate the turbulence dissipation rate of a flow even when the size of the interrogation volume in the PIV measurement is much larger than the Kolmogorov length scale. We found that a sharp-cut low-pass filter for the energy spectrum, which has been used till date, does not represent the correct nature of the spatial averaging that a PIV interrogation volume performs onto the true velocity field. To this end, we mathematically derived a PIV equivalent low-pass filter, and then applied it to the volumetric PIV results that we obtained after performing phase-locked tomographic PIV measurements inside a stirred flow mixer. The subgrid-stress model that we used is a modified Smagorinsky model that is recently proposed by Meyers and Sagaut (J. Meyers and P. Sagaut, “On the model coefficients for the standard and the variational multi-scale Smagorinsky model,” *Journal of Fluid Mechanics*, Vol.569, pp.287-319, 2006). We found that the dissipation rate directly calculated from the PIV measured velocity field is underestimated by two order of magnitudes compared to the modeled dissipation rate.

INTRODUCTION

A direct measurement of turbulence dissipation rate has been a challenging task till date, due to the requirement to simultaneously measure all the three velocity components with sufficiently high spatial resolution. This is an essential requirement, which is dictated by the fact that the expression of dissipation rate, $\epsilon = \frac{1}{2}\gamma\sum_i\sum_j\left(\frac{\partial U_i}{\partial x_j}+\frac{\partial U_j}{\partial x_i}\right)^2$, contains spatial derivative terms, which requires all the small scale motions comparable to the Kolmogorov length scales well resolved. One of the common approaches that researchers have been taking in past is to use the hot-wire technique to obtain high time-resolution velocity data at a given point in space (for gaseous flows), then transform the time-series data into a one-dimensional spatial data series after considering the turbulence passing the probe to be frozen, obtain the one-dimensional spatial derivatives from the transformed data, and then assume that all the spatial derivatives required in the calculation of the dissipation rate are equal. Many times, additional assumptions, such as, existence of homogeneity and isotropy, are also made. Although this approach can be used to calculate the dissipation rate, its accuracy is often not good enough to reliably use the results in a practical application. More or less the same method is also applied on LDV time-series data for measurements inside a liquid medium.

After the development of Particle Image Velocimetry (PIV) measurement technique to obtain the flow velocity in a spatial region, instead of at a point, some researchers carried out measurements after magnifying a small spatial region of the flow, in order to obtain velocity fields with high spatial resolutions, so that the motions comparable to the Kolmogorov length scale can be resolved and the turbulence dissipation rate can be calculated, accurately. However, this approach, till date, has been limited only to measurements in planes (instead of in volumes), which, in general, cannot be used to calculate all the nine spatial derivative components which are required for the calculation of the dissipation rate. In order to overcome this limitation, the extra spatial derivatives are often approximated, which, again, does not yield a good enough value of the dissipation rate that can be used in practical applications. In some particular cases, however, the two-dimensional PIV measurements can be reliably used together with assumption of locally axisymmetric turbulence [1,2], to calculate the dissipation rate. George and Hussein [3] discussed usefulness of the locally axisymmetric turbulence and provided expressions for the calculation of dissipation rate from two-dimensional velocity data, provided that the local axis of the symmetry is known.

Recently, Tomographic PIV [4,26] has emerged as a reliable technique to measure all the three flow velocity components inside a volume. Although this technique has been applied in many scenarios, including those by us [5,6], a magnified measurement that can resolve even the small scale motions appears difficult. This is because the depth of field of the viewing cameras, which limits thickness of the measurement volume, decreases when the camera lens is zoomed to magnify a small region of interest, thereby making a magnified volumetric measurement unfeasible for the extent of the magnification that is required to well resolve the small scale motions.

Given the aforementioned difficulties in reliable direct measurement of the turbulence dissipation rate, we, in this paper, have thoroughly elaborated a technique based on subgrid-stress modeling, which is the basis of Large Eddy Simulations (LES), in order to enable a reliable estimation of the turbulence dissipation rate even in the cases where the resolved spatial scales cannot capture the small scale motions. It will be apparent shortly that this idea of using the subgrid-stress model in the context of PIV is not completely new in itself. However, important details that can greatly affect the accuracy of the modeled dissipation rate, as well as a formal description of the similarity between the PIV measured results and the subgrid-stress model have been missing. In the present study, we worked out these details and applied the model to the experimental results that we obtained after performing a phase-locked tomographic PIV measurement inside a stirred flow mixer. Note that the turbulence dissipation rate inside a mixer has not been reliably estimated yet, despite several attempts in past, which used both the numerical and experimental techniques [7-11]. The knowledge of the dissipation rate directly affects efficiency of the mixers.

The idea of the subgrid-stress modeling can be applied to PIV results because the instantaneous velocity vectors that a PIV measurement yields are essentially velocity vectors spatially averaged over the interrogation volume, which is qualitatively similar to the approach taken in the subgrid-stress modeling in LES simulations where the Navier-Stokes equations are solved after volume averaging them over the computational cells. There is an important, but often overlooked, difference between the two types of the averaging. In LES simulations, the space-averaging is usually performed by subjecting the energy spectrum to some type of low-pass filter, which removes contributions of the high wavenumber components. Since the energy spectrum of a to-be-investigated flow are not known beforehand, it is modeled, often as an isotropic spectrum. One of the isotropic spectra that is widely used in LES simulations is Pope's spectrum, because it is known to exhibit good similarities with many realistic flows [12]. Since the low-pass filtering of the energy spectrum is qualitatively similar to the low-pass filtering performed on the spectrum of the three individual velocity components, the LES filtering essentially yields spatially averaged velocity components. This averaging, in general, happens to be a weighted averaging, which is different from the simple non-weighted averaging that the PIV interrogation volume performs on the true flow velocity field. Therefore, in order to achieve the ideal similarity between the LES filtering and the PIV averaging, we need to select an appropriate low-pass filter for the energy spectrum, so that its effect on the velocity components is the simple spatial averaging (and not the weighted averaging).

In LES simulations, one of the models that is well documented and has been often used is the classical Smagorinsky model [13, 14], which uses the isotropic inertial-range spectrum $\left(\xi(k) = \alpha \epsilon^{2/3} k^{-5/3};\ \alpha \text{ is a constant}\right)$ and assumes that the low-pass filter is an isotropic sharp-cut filter with the cutoff wavenumber $k_c = \pi/\Delta$. Sheng el al [15] were probably the first who tried to apply a subgrid-stress model to a PIV result to obtain turbulence dissipation rate of a flow. They applied the classical Smagorinsky model to the two-dimensional PIV results that they obtained for a stirred flow mixer (while accounting the unmeasured velocity gradients through some approximations). Note that although the classical Smagorinsky model can be readily applied to the PIV measurement results, most of the times it yields an incorrect value of the dissipation rate, because (1) it requires the turbulence Reynolds number to be extremely large, which is often not true in many practical cases (2) it requires the size of the interrogation window to fall in the inertial subrange of the energy cascade [15], and (3) it assumes an isotropic sharp-cut filter in the wavenumber domain, which is not equivalent to the spatial averaging that a PIV interrogation volume performs on the velocity field (we will discuss this issue in detail in this paper). Alekseenko et al [17] assumed Pao's spectrum $\left(\xi(k) = \alpha \epsilon^{2/3} k^{-5/3} \exp\left(-\frac{3}{2}\alpha (k\eta)^{4/3}\right);\ \alpha \text{ is a constant}\right)$ [18] as the energy spectrum, which is valid in the entire equilibrium range (including that in the dissipation range). In a later study, Alekseenko et al [11] used a modified Smagorinsky model, which is recently proposed by Meyers and Sagaut [19] and is based on the much more realistic Pope's spectrum $\xi(k) = \alpha \epsilon^{2/3} k^{-5/3} \cdot f_L(kL) \cdot f_\eta\left(kLRe_L^{-3/4}\right)$ where $f_L(x) = \left(1 + c_L x^{-2}\right)^{-11/6}$, $f_\eta(x) = \exp\left(-c_\beta c_\eta\left(\left[x^4 c_\eta^{-4} + 1\right]^{1/4} - 1\right)\right)$, and α, c_L, c_β, and c_η are constants. This model takes into account not only the dissipation that occurs due to the turbulence viscosity at the subgrid scales, but also the direct dissipation due to the fluid's viscosity at the resolved scales. Furthermore, this model works well for all values of Δ in the equilibrium range. In both these studies, Alekseenko et al [11,17] assumed the isotropic sharp-cut filter with the cutoff wavenumber $k_c = \pi/\Delta$. Since Alekseenko et al [11,17] used the energy spectrum that are closer to the reality than the inertial-range spectrum, the results obtained in their studies are expected to be more accurate than if the classical Smagorinsky model had been used. In fact, when Alekseenko et al [17] compared the theoretical value that they obtained for the turbulence dissipation rate (after assuming Pao's spectrum) with the dissipation rate directly calculated from magnified stereo PIV measurement results (for a swirling impinging jet flow), they found that the two values match well when the interrogation window size in the PIV experiments is equal to about 7 times the Kolmogorov length scale. Here, note that although the theoretical and the experimental values matched well in this particular case for small interrogation window sizes, (1) use of the isotropic filter for a non-isotropic PIV interrogation window and (2) use of a sharp-cut filter to represent the spatial averaging performed by the PIV interrogation window, both remain unjustified, which, in turn, hampers general accuracy of the model.

According to Willert and Gharib [20] and Foucaut et al [21], the highest resolved wavenumber in a two-dimensional PIV measurement is equal to π/Δ, where $\Delta x = \Delta y = \Delta$ is the side-length of the interrogation window. In the volumetric PIV measurements, it would be the side-length of the interrogation volume. This is perhaps the reason why, till date, the isotropic sharp-cut filter with cutoff wavenumber equal to π/Δ has been used when a subgrid-stress model is applied to PIV results. However, shortly, we will see that an isotropic sharp-cut filter does not have the same space averaging effect that the interrogation window/volume in PIV measurements performs onto the velocity field.

NOMENCLATURE

B		Box function
D	[mm]	Diameter of the impeller (90 mm in the present study)
E	[mm^2/s^2]	Kinetic energy of a flow
i, j	[-]	Indices representing the three spatial directions. Their values may be 1, 2, and/or 3, which, represent a quantity in the X, Y, and/or Z direction, respectively; e.g. $U_1 = U$, $U_2 = V$, $U_3 = W$, etc.
k	rad/m	Wave number in the Fourier space
L	m	Integral length scale
Re	[-]	Reynolds number ($\equiv \omega D^2/2\gamma$ in the present study)
t	[s]	Time
X	[mm]	Horizontal axis in the rightward direction, with the origin lying on the tip of the rotating shaft
Y	[mm]	Vertical axis in the upward direction, with the origin lying on the tip of the rotating shaft
Z	[mm]	Direction perpendicular to the X-Y plane, considering a right-handed Cartesian coordinate system
U, V, W	[mm/s]	X, Y, and Z components of the instantaneous flow velocity
u, v, w	[mm/s]	Turbulence fluctuations in the U, V, and W components of the velocity, respectively; $u \equiv U - \overline{U}$ etc.

Special characters

γ	[mm^2/s]	Kinematic viscosity of the working fluid
γ_t	[mm^2/s]	Turbulence viscosity
Δ	[mm]	Side-length of the interrogation volume (2 *mm* in the present study)
ε	[mm^2/s^3]	Turbulence dissipation rate
η	[mm]	Kolmogorov length scale
ξ		Energy spectrum
φ	[degree]	Phase angle (angular location of the mid-plane of the measured axisymmetric volume sheet)
ω	[rad/s]	Impeller's rotation speed in the clockwise direction (150 *RPM* or 15.7 *rad/s*)
ρ	[kg/m^3]	Density

Abbreviations

PIV	Particle Image Velocimetry
LES	Large Eddy Simulation
RMS	Root Mean Square
TKE	Turbulence Kinetic Energy

Conventions

a^*	A physical quantity a in its non-dimensional form
$\overline{a}$	Time-averaged value of a physical quantity a
$\tilde{a}$	Space-averaged value of a physical quantity a
F_a	Fourier transform a physical quantity a
$a \circ b$	Convolution of two physical quantities a and b

Normalization

In this study, many physical quantities are presented in non-dimensional forms, due to their practical importance. The non-dimensional quantities are indicated by an asterisk mark (*), and they are defined at the place of their first use.

In the following of this paper, first we will describe the subgrid-stress model in the context of volumetric PIV. In order to do that, we will first theoretically obtain a PIV-equivalent low-pass filter for the energy spectrum. Thereafter, we will obtain analytic expressions for the subgrid-stress model that can be readily used with volumetric PIV results. Afterwards, we will provide a brief description of our tomographic PIV experiment. In the end, we will compare the turbulence dissipation rate that is directly calculated from the PIV measured velocity field and the dissipation rate obtained after application of the subgrid-stress model, followed by drawing conclusions.

SUBGRID STRESS MODEL IN CONTEXT OF PIV

PIV-equivalent low pass filter for energy spectrum

A space-averaged instantaneous velocity field obtained from a PIV measurement is equivalent to the convolution of the true flow velocity field and a box filter of side-lengths equal to the side-lengths of the PIV interrogation volume. We have made this scenario clear by a schematic diagram in Figure 1(a), which shows convolution of a hypothetical, one-dimensional velocity field with the box function. The diagram shows that the variations in the true velocity field are somewhat flattened out by the one-dimensional box function. This process is also called smoothing, filtering, or averaging. In a similar fashion, the interrogation volume in a volumetric PIV experiment also averages out variations in the true flow velocity field, through the three-dimensional box function, $B(x,y,z)$. Mathematically, this box function and the averaged velocity, respectively, can be written (in terms of the convolution) as follows:

$$B(x, y, z) = \frac{1}{\Delta x \cdot \Delta y \cdot \Delta z} \times \begin{cases} 1, & \text{if } |x| \le \Delta x/2,\ |y| \le \Delta y/2, \text{ and } |z| \le \Delta z/2; \\ 0, & \text{otherwise;} \end{cases} \tag{1}$$

$$\tilde{U}(x, y, z) = \frac{1}{\Delta x \cdot \Delta y \cdot \Delta z} \int_{-\frac{\Delta x}{2}}^{\frac{\Delta x}{2}} \int_{-\frac{\Delta y}{2}}^{\frac{\Delta y}{2}} \int_{-\frac{\Delta z}{2}}^{\frac{\Delta z}{2}} U(x+x', y+y', z+z')\, dx'\, dy'\, dz'$$

where Δx, Δy, and Δz are the side-lengths of the box function, in the directions X, Y, and Z, respectively; and $U(x, y, z)$ and $\tilde{U}(x, y, z)$ are a true velocity component and its averaged value, respectively.

Since the convolution of two spatial functions in the physical domain is equivalent to multiplication of their Fourier transforms in the wavenumber domain, the above filtering process can also be realized by first taking Fourier transforms of the box function and the true velocity field, individually, multiplying them, and then taking the inverse Fourier transform of the multiplied velocity field. Here, the Fourier transform $F_B(k_1,k_2,k_3)$ of the box function B(x,y,z) is the well-known three-dimensional *sinc* function, which can be given as below:

$$F_B(k_1, k_2, k_3) = \frac{\sin(k_1 \Delta x/2)}{(k_1 \Delta x/2)} \cdot \frac{\sin(k_2 \Delta y/2)}{(k_2 \Delta y/2)} \cdot \frac{\sin(k_3 \Delta z/2)}{(k_3 \Delta z/2)} \tag{2}$$

where k_1, k_2, and k_3 are the three wavenumbers in the Fourier space. The definition of the Fourier transform F_B is given as

$$F_B(k_1, k_2, k_3) = \int_{-\infty}^{+\infty} \int_{-\infty}^{+\infty} \int_{-\infty}^{+\infty} B(x, y, z) \cdot \exp(-ik_1 x - ik_2 y - ik_3 z)\, dx\, dy\, dz.$$

Later, a similar definition is adopted even for Fourier transform of other physical quantities.

The kinetic energy of the flow that is obtained from the PIV-measured velocity field can be written as

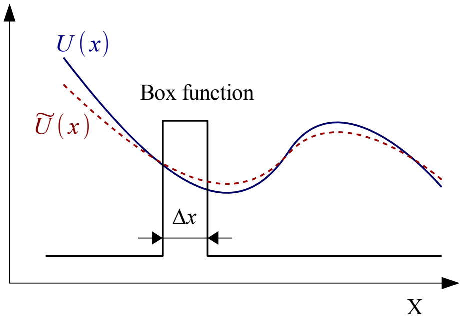

Figure 1(a) A schematic diagram showing averaging (or flattening) of a one-dimensional velocity field, $U(x)$, by a one-dimensional box function. Here, $\widetilde{U}(x)$ represents the averaged value.

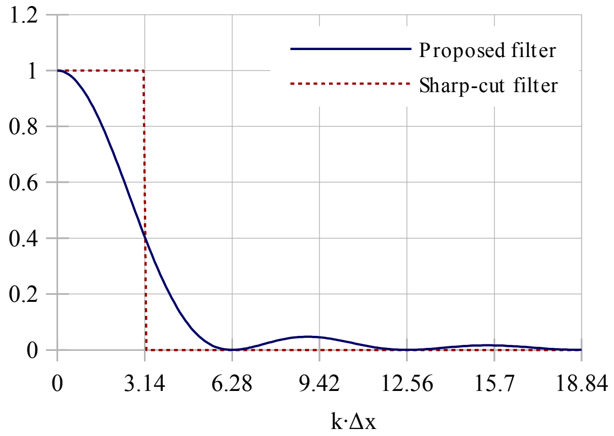

Figure 1(b) One-dimensional low-pass filter $F_C = [\sin(k\cdot\Delta x/2)/(k\cdot\Delta x/2)]^2$ and the sharp-cut filter with the cutoff wavenumber equal to $\pi/\Delta x$.

$$E^{(\mathrm{PIV})} = \frac{1}{2}\left[\widetilde{U}^2 + \widetilde{V}^2 + \widetilde{W}^2\right] = \frac{1}{2}\left[(U \circ B)^2 + (V \circ B)^2 + (W \circ B)^2\right] \qquad (3)$$

where the small circle between any two variables represent their convolution. Alternatively, we can also write $E^{(\mathrm{PIV})}$ as

$$E^{(\mathrm{PIV})} = \frac{3}{(2\pi)^3}\int_0^\infty\int_0^\infty\int_0^\infty \xi^{(\mathrm{PIV})}\, dk_1\, dk_2\, dk_3 \qquad (4(a))$$

where $\xi^{(\mathrm{PIV})}$ is the energy spectrum corresponding to $E^{(\mathrm{PIV})}$. Mathematically, $\xi^{(\mathrm{PIV})}$ can be written as

$$\xi^{(\mathrm{PIV})} = \frac{1}{2}\left(|F_{\widetilde{U}}|^2 + |F_{\widetilde{V}}|^2 + |F_{\widetilde{W}}|^2\right) \qquad (4(b))$$

where $|F_{\widetilde{U}}|$, $|F_{\widetilde{V}}|$, and $|F_{\widetilde{W}}|$ are the amplitudes of the Fourier transforms of the PIV measured velocity components $\widetilde{U}$, $\widetilde{V}$, and $\widetilde{W}$, respectively.

The low-pass filter that we intend to apply on the energy spectrum should also yield the same value of the kinetic energy as the PIV does. Therefore, if we represent this low-pass filter in the physical domain by a function $C(x,y,z)$, and its Fourier transform by F_C, we can write $E^{(\mathrm{PIV})}$ as follows:

$$E^{(\mathrm{PIV})} = \frac{3}{(2\pi)^3}\int_0^\infty\int_0^\infty\int_0^\infty \xi\, F_C\, dk_1\, dk_2\, dk_3 \qquad (5(a))$$

where ξ is the energy spectrum based on the true velocity field (U, V, W). Similar to $\xi^{(\mathrm{PIV})}$, ξ can also be written in terms of the amplitudes of the Fourier transforms of the true velocity components, as follows:

$$\xi = \frac{1}{2}\left(|F_U|^2 + |F_V|^2 + |F_W|^2\right) \qquad (5(b))$$

From equations (4(a)) and (5(a)), it follows that $\xi^{(\mathrm{PIV})} = \xi F_C$. With the help of equations (4(b)) and (5(b)), we can write $F_C = \frac{\xi^{(\mathrm{PIV})}}{\xi} = \frac{|F_{\widetilde{U}}|^2 + |F_{\widetilde{V}}|^2 + |F_{\widetilde{W}}|^2}{|F_U|^2 + |F_V|^2 + |F_W|^2}$. Now, we substitute $F_{\widetilde{U}} = F_U F_B$ etc. (where F_B is the Fourier transform of the box function B(x,y,z); see equation (2)) and obtain the following:

$$F_C = \frac{|F_U F_B|^2 + |F_V F_B|^2 + |F_W F_B|^2}{|F_U|^2 + |F_V|^2 + |F_W|^2} = |F_B|^2$$

Since F_B is an spectral function with phase angle equal to 0 (see equation (2)), we can write $F_C = F_B^2$; or,

$$F_C(k_1, k_2, k_3) = \left[\frac{\sin(k_1\Delta x/2)}{(k_1\Delta x/2)}\cdot\frac{\sin(k_2\Delta y/2)}{(k_2\Delta y/2)}\cdot\frac{\sin(k_3\Delta z/2)}{(k_3\Delta z/2)}\right]^2 \qquad (6)$$

In order to show difference between the sharp-cut filter and the derived filter F_C, we plot them in Figure 1(b), in one wavenumber direction. The figure clearly shows that the two functions are very different from each-other.

Since $F_C = F_B^2$ is equivalent to $C = B \circ B$ in the physical domain, it is easy to show that the function $C(x,y,z)$ would be a *triangular* function; whereas, for a sharp cut filter, $C(x,y,z)$ would be a *sinc* function.

The subgrid-stress model

In the present study, we will use a subgrid-stress model that is primarily based on the modified Smagorinsky model proposed by Meyers and Sagaut [19]. According to them, the turbulence viscosity γ_t can be given as

$$\gamma_t = \left(\left(\frac{C_{s,\infty}\Delta}{\zeta}\right)^4\left(2\sum_i\sum_j \overline{S_{ij}^{(\mathrm{PIV})} S_{ij}^{(\mathrm{PIV})}}\right) + \gamma^2\right)^{\frac{1}{2}} - \gamma \qquad (7)$$

where (i) $\Delta x = \Delta y = \Delta z = \Delta$, (ii) $C_{s,\infty}$ is the Smagorinsky constant in the classical subgrid stress model and it is equal to 0.173, as obtained by Lilly [14], (iii) ζ is a constant that depends on the type and shape of the low-pass filter, and (iv) $S_{ij}^{(\mathrm{PIV})} = \frac{1}{2}\left(\frac{\partial \widetilde{U}_i}{\partial x_j} + \frac{\partial \widetilde{U}_j}{\partial x_i}\right)$ is the strain rate tensor directly calculated from the PIV measured velocity field. The expression (7) is based on Pope's spectrum [12], and takes into account the energy dissipation both at the subgrid scales and at the resolved scales. Meyers and Sagaut [19] provided values of ζ for some commonly used low pass filters, such as, for the *isotropic* sharp-cut filter with the cutoff wavenumber equal to π/Δ, it is equal to 1; and for the *cubical* sharp-cut filter with the cutoff wavenumber equal to π/Δ in all the three wavenumber directions, the value is equal to 1.22. Since we will use the cubical function given by equation (6), we need to explicitly calculate the value of ζ, as outlined below.

For any general three-dimensional low-pass filter $G(k)$, Meyers and Sagaut [19] provided an explicit mathematical expression in the spherical coordinate system, to calculate the value of ζ, which can be written as

$$\zeta = \left[\frac{1}{3\pi}\int_0^\infty\int_0^{2\pi}\int_0^{\pi} k^{\frac{1}{3}}\{G(\vec{k})\}^2 \sin(\theta)\, d\theta\, d\varphi\, dk\right]^{\frac{3}{4}} \times \frac{\Delta}{\pi}.$$

Since we will use a cubical filter in this study (not an isotropic filter; see equation (6)), we transform the above expression into the Cartesian coordinate system, for easy calculation, as follows:

$$\zeta = \left[\frac{8}{3\pi} \int_0^\infty \int_0^\infty \int_0^\infty \left(\alpha_1^2 + \alpha_2^2 + \alpha_3^2 \right)^{\frac{-5}{6}} \left\{ H\left(\alpha_{1,} \alpha_{2,} \alpha_3\right) \right\}^2 d\,\alpha_1\, d\,\alpha_2\, d\,\alpha_3 \right]^{\frac{3}{4}} \quad (8)$$

where $|\vec{k}|^2 = k_1{}^2 + k_2{}^2 + k_3{}^2$; $\alpha_i = k_i\Delta/\pi$, $i = 1,2,3$; and $H(\alpha_1,\alpha_2,\alpha_3)$ is the filtering function equivalent to $G(k_1,k_2,k_3)$. In the present study, $G(k_1,k_2,k_3) = F_C(k_1,k_2,k_3)$, which is given by equation (6); and, therefore, $H(\alpha_1,\alpha_2,\alpha_3)$ can be written as

$$H\left(\alpha_{1,} \alpha_{2,} \alpha_3\right) = \left[\frac{\sin\left(\pi\alpha_1/2\right)}{\left(\pi\alpha_1/2\right)} \cdot \frac{\sin\left(\pi\,\alpha_2/2\right)}{\left(\pi\,\alpha_2/2\right)} \cdot \frac{\sin\left(\pi\alpha_3/2\right)}{\left(\pi\alpha_3/2\right)} \right]^2 \quad (9)$$

We numerically evaluated the expression (8), for $H(\alpha_1,\alpha_2,\alpha_3)$ given by equation (9), and obtained $\zeta = 0.70$, which is only about 58% of the value in the case of the isotropic sharp-cut filter. Since the turbulent viscosity is inversely proportional to the square of ζ (see equation (7)), the reduced value of ζ would amplify the value of the modeled dissipation rate to about three times the rate obtained by assuming the isotropic sharp-cut filter.

Now, with the full knowledge of γ_t, the dissipation rate directly calculated from the PIV measured velocity field and that calculated using the subgrid-stress model can be given as

$$\epsilon^{(\mathrm{PIV})} = 2\gamma \sum_i \sum_j \overline{S_{ij}^{(\mathrm{PIV})} S_{ij}^{(\mathrm{PIV})}} \quad (10(a)) \text{ and}$$

$$\epsilon = 2\gamma_t \sum_i \sum_j \overline{S_{ij}^{(\mathrm{PIV})} S_{ij}^{(\mathrm{PIV})}} \quad (10(b)),$$

respectively. From here, we obtain $\varepsilon = \gamma_t{\cdot}\varepsilon^{(\mathrm{PIV})}/\gamma$. In the normalized form, we can write the modeled dissipation rate, ε^*, as follows:

$$\epsilon^* = \frac{\gamma_t}{\gamma}\, \epsilon^{(\mathrm{PIV})*} \quad (11(a))$$

$$\frac{\gamma_t}{\gamma} = \left(\left(\frac{C_{s,\infty}\Delta^*}{\zeta} \right)^4 Re^3\, \epsilon^{(\mathrm{PIV})*} + 1 \right)^{\frac{1}{2}} - 1, \quad (11(b))$$

$$\epsilon^{(\mathrm{PIV})*} = \frac{2}{Re} \sum_i \sum_j \overline{S_{ij}^{(\mathrm{PIV})*} S_{ij}^{(\mathrm{PIV})*}}, \quad (11(c))$$

$$S_{ij}^{(\mathrm{PIV})*} = \frac{1}{2}\left(\frac{\partial \tilde{u}_i^*}{\partial x_j^*} + \frac{\partial \tilde{u}_j^*}{\partial x_i^*} \right), \quad (11(d))$$

where $C_{s,\infty} \approx 0.173$, $\zeta = 0.70$, ε and $\varepsilon^{(\mathrm{PIV})}$ are normalized with respect to $\omega^3 D^2/8$, and Δ is normalized with respect to D.

We will use the set of equations (11(a))~(11(d)) to calculate the modeled turbulence dissipation rate, ε^*. Note that in equation (11(d)), we have replaced the gradients of the PIV measured velocity components $\widetilde{U}_i$ with the gradient of the measured velocity fluctuation components $\tilde{u}_i$ (mathematically, $\tilde{u}_i = \widetilde{U}_i - \overline{\widetilde{U}_i}$), which is fairly acceptable, because the velocity fluctuation gradients in turbulent flows happen to be overwhelmingly larger than the mean velocity gradients.

FLOW DOMAIN AND EXPERIMENTAL DETAILS

Although the flow geometry and the Tomographic PIV experiment are same as that in our previous studies [5,6], we will brief them here for completion purposes.

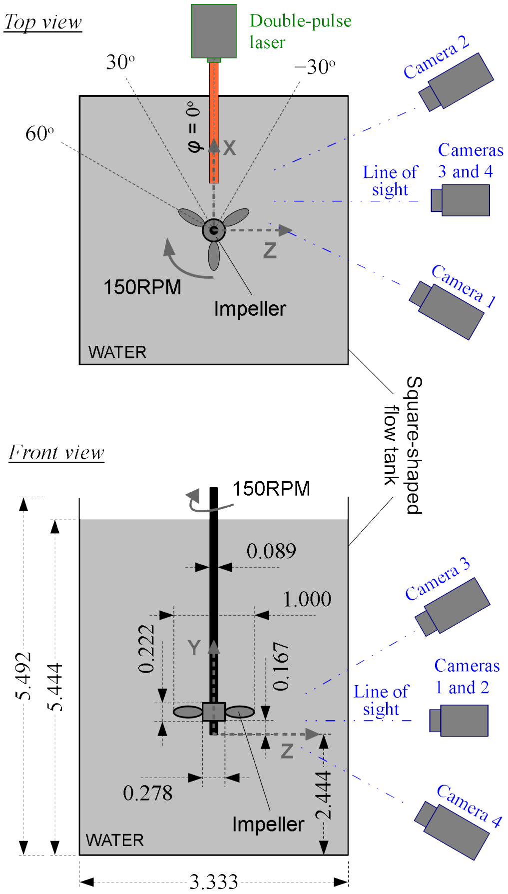

Figure 3 Schematic diagrams of the flow domain, with the spatial dimensions normalized with respect to the impeller diameter, D. The camera positions are also shown.

The flow domain consists of a square-shaped cylindrical tank, filled with water, with a rotating HR-100 impeller [23] acting as the agitator. The impeller is mounted on a thin, round shaft and placed along the central axis of the tank, and driven by an electric motor with the angular speed of 150 RPM; i.e. $\omega = 15.7$ *rad/s*, in the clockwise direction when viewed from the top. Schematic diagrams of the flow geometry and the experimental arrangement are shown in Figure 3. The figure also contains the right-handed Cartesian coordinate system that is used in the present study. The HR-100 impeller is shown in Figure 4. The diameter of the impeller $D = 90$ *mm*.

We carried out phase-locked measurements in 7 *mm* thick vertical volume sheets, at four different angular locations, as shown in the top view of Figure 3. We refer the angular locations of the mid-planes of the measurement volume sheets as *phase angles* (φ), where $\varphi = 0$° aligns with the front hole of the two screw-holes (when the impeller rotates) that are there on the hub of the impeller. It lies approximately in the middle of two of the three identical impeller blades. We performed all the measurements at the water temperature of 19°C. The corresponding Reynolds number $Re = \omega D^2/2\gamma = 59400$.

Before the acquisition of the particle images, we carried out a precise camera calibration using a calibration plate with

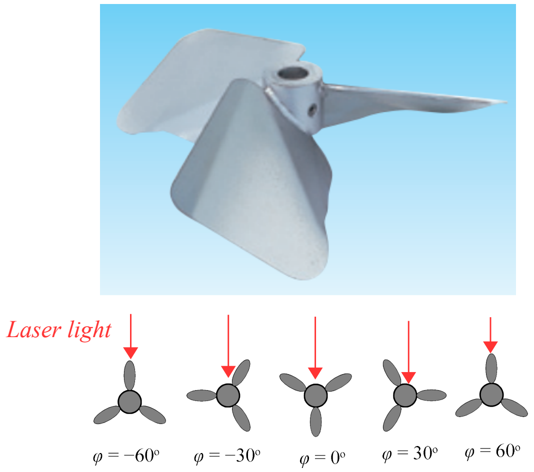

Figure 4 The HR-100 impeller [23], which is used in the present study as the agitator. The figure also shows schematic diagrams of the top views of the impeller at different phase angles.

circular dots of diameter 2 *mm* printed on it. The calibration plated was aligned parallel to the viewing wall of the flow domain, and the dimensional accuracy of the printed dots were better than 10 μm. We used four CCD cameras (of resolution 1600×1200 *pixel*^{2}) to acquire the images of the calibration plate, from four different angles. The cameras were arranged in a *plus* (+) configuration, and the angle that the line of sight of the cameras made with the normal of the viewing wall was about 25°. The Scheimpflug condition, in order to sharply visualize the images, is realized by using two commercially-available perspective-controlled lenses and two lensbaby. We could obtain nearly circular images (not elliptical) of the dots, followed by obtaining both the intrinsic and the extrinsic camera parameters using the pin-hole camera model. The average projection error based on these camera parameters was less than 0.5 *pixels* (for each camera), which is within acceptable limits [4].

We seeded the flow with spherical Nylon particles of average diameter 10 μm, and illuminate them with a double-pulse Nd:YAG laser of energy output equal to 30 *mJ/pulse*. At each of the four phase angles, we acquired a total of 3000×4 pairs of the particle images, and analyzed them with a self-developed GPU program (written in the CUDA programming language), in order to obtain a total of 3000 pairs of the instantaneous velocity fields. The size of the interrogation volume was 48×48×48 *voxel*^{3}, which translates to 2×2×2 *mm*^{3} in the physical coordinates. The overlap ratio of the interrogation volumes was 50%, which yielded the instantaneous velocity vectors separated by 1 *mm*. We removed spurious velocity vectors obtained from the instantaneous velocity fields by using a statistical method propose by Thompson [24]. Essentially, this method recognizes an instantaneous velocity vector (at a given spatial point) as a spurious vector if magnitude of the instantaneous velocity fluctuation at that time instant exceeds a predefined limit, which we set equal to three times the standard deviation of the velocity at that spatial point. The erroneous velocity vectors are subsequently ignored.

EXPERIMENTAL AND MODELED DISSIPATION RATES

We used the set of equations (11(a))~(11(d)) to calculate the modeled value of the turbulence dissipation rate, ε^*. First, we calculated all the $\overline{S_{ij}^{(\mathrm{PIV})*}S_{ij}^{(\mathrm{PIV})*}}$ components, individually, by using equation (11(d)), and them summed them to obtain $\varepsilon^{(\mathrm{PIV})*}$. Since the overlap ratio of the interrogation volume in our Tomographic PIV measurement is 50%, we used the standard 2nd order central-difference method in the calculation of the $S_{ij}^{(\mathrm{PIV})*}$, because, according to Foucaut and Stanislas [22], it is the most suitable discretization method for 50% overlap ratio. Note that computation of the individual $\overline{S_{ij}^{(\mathrm{PIV})*}S_{ij}^{(\mathrm{PIV})*}}$ components (followed by summing them up) has favorable consequences, because computation of an $S_{ij}^{(\mathrm{PIV})*}$ component requires only four valid neighboring vectors to be present in any instantaneous velocity field. On the other hand, a direct calculation of $\varepsilon^{(\mathrm{PIV})*}$ requires six valid neighboring vectors, which is a stricter requirement, and therefore the total number of the error-free PIV data samples that can be used in the calculation reduces (which, in turn, degrades the quality of the dissipation rate).

The directly calculated turbulence dissipation rate, $300\times\varepsilon^{(\mathrm{PIV})*}$, is plotted in Figures 5(a)~(d), for the phase angles −30°, 0°, 30°, and 60°, respectively. The dissipation rate is normalized with respect to $\omega^3D^2/8$. The spatial dimensions in the plots are normalized with respect to the impeller diameter, *D*. Similarly, the normalized values of the modeled dissipation rate, ε^*, are plotted in Figures 6(a)~(d), respectively. Note that the spatial direction Z^* in these figures is expanded out of proportion, for visual clarity. The magnitudes in the former set of the figures (Figures 5(a)~(d)) are multiplied by 300 to make them comparable to the magnitudes of the modeled dissipation rate, for easy comparison. The directly calculated dissipation rate, $\varepsilon^{(\mathrm{PIV})*}$, is hugely underestimated due to the size of the interrogation volume being much larger than the Kolmogorov length scale ($\Delta \approx 62.50\eta$, as we will see shortly). The plots also show that, despite the large differences in the magnitudes of the directly calculated and the modeled turbulence dissipation rates, their distribution patterns remain approximately same.

The spots of large magnitudes in the middle of the Figures 5(b), 5(c), 6(b), and 6(c) correspond to the tip-vortices that the rotating blades generate (which we previously reported elsewhere, in detail [5, 6, 16, 25]). Such vortices are also commonly observed in wind turbines, where they extend till tens of diameters in the wake of the rotating fan. In the present case, however, they diffuse quickly (see figures 5(a) and 6(a)), because the viscosity of the working fluid, water, is much higher than that of the air. Note that, since the blade in Figures 5(a) and 6(a) is just cutting the measurement region, the newly formed vortices are not apparent yet.

A careful comparison of the two sets of the figures also reveals that the subgrid-stress model amplifies the turbulence dissipation rate more in the core of the vortex than outside it, perhaps due to the higher turbulence level found in the core region where the Kolmogorov length scale is likely smaller. At

(a) Phase angle = −30°

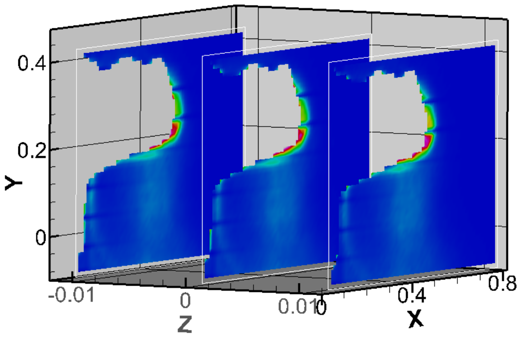

(b) Phase angle = 0°

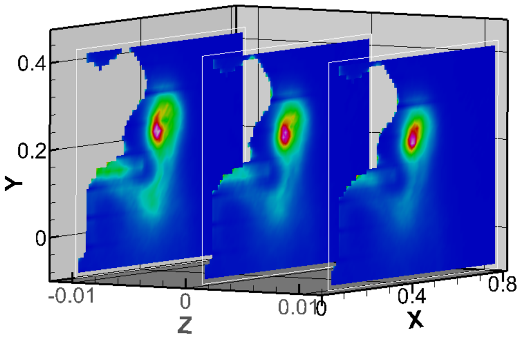

(c) Phase angle = 30°

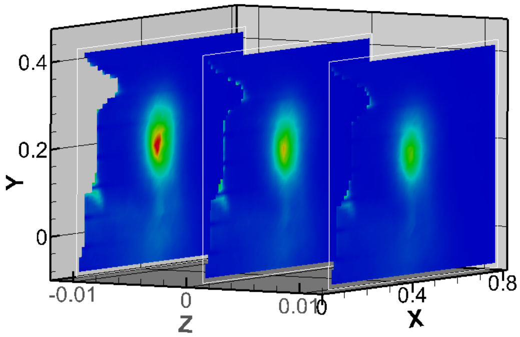

(d) Phase angle = 60°

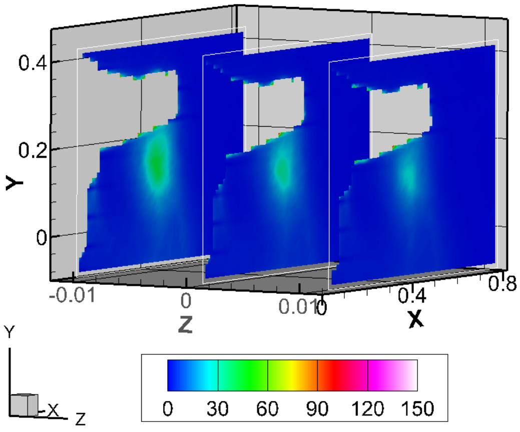

Figure 5 The directly calculated turbulence dissipation rate, $300\times\varepsilon^{(PIV)*}$, at the four different phase angles. All the spatial dimensions are normalized w.r.t. the impeller diameter, *D*.

(a) Phase angle = −30°

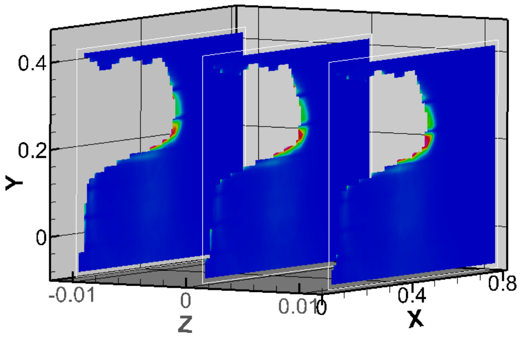

(b) Phase angle = 0°

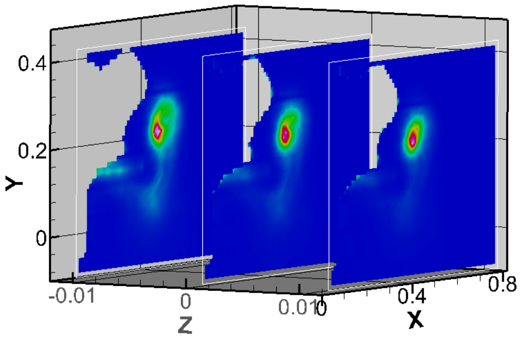

(c) Phase angle = 30°

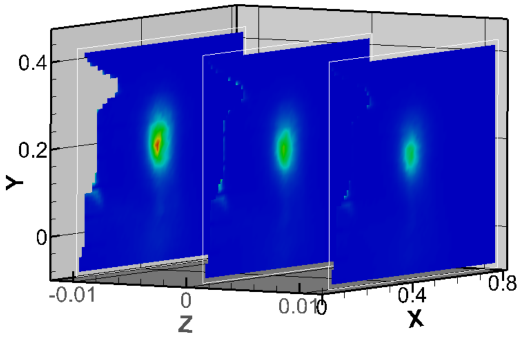

(d) Phase angle = 60°

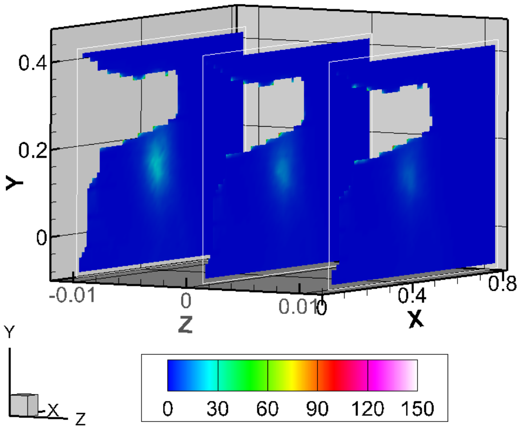

Figure 6 The true turbulence dissipation rate, ε^{*}, at the four different phase angles. All the spatial dimensions are normalized w.r.t. the impeller diameter, *D*.

such places, the dissipation rate spectrum happens to be concentrated about a higher wavenumber (than at the places of larger Kolmogorov length scale), and therefore a given interrogation volume in a PIV experiment underestimates the dissipation rate more.

In order to have some qualitative idea of inaccuracy in the modeled turbulence dissipation rate compared to the true value, we calculated nominal values of the Kolmogorov length scale and the integral length scale in the core of the vortex (because, here, the turbulence level is maximum). To this end, we first set nominal value of the turbulence dissipation rate, $\varepsilon^*_{\text{nom}}$, equal to the magnitude of the turbulence production rate, which is equal to about 0.3 in the vortex core at the phase angles 0° and 30° (as we reported elsewhere [6]). For this value, nominal value of the Kolmogorov length scale can be given as $\eta^*_{\text{nom}} = \left(Re^3 \epsilon^*_{\text{nom}}\right)^{-1/4} = (59400^3 \times 0.3)^{-0.25} = 3.55\times10^{-4}$. Similarly, we also calculated nominal value of the integral length scale as $L^*_{\text{nom}} = \left(\frac{2}{3}\times TKE^{(\text{PIV})*}\right)^{\frac{3}{2}}\left(\frac{1}{\epsilon^*_{\text{nom}}}\right) = \left(\frac{2}{3}\times 0.1\right)^{\frac{3}{2}}\left(\frac{1}{0.3}\right) = 573.78\times10^{-4} = 161.63\eta^*_{\text{nom}}$ where the turbulence kinetic energy directly calculated from the PIV measured velocity fluctuations, $TKE^{(\text{PIV})*}$, is also taken from our previous studies [5,6]. In dimensional forms, $\eta_{\text{nom}} = \eta^* D = 3.20\times10^{-2}$ *mm* and $L_{\text{nom}} = L^* D = 5.16$ *mm*. Therefore, the side-length of the interrogation volume, Δ (which is equal to 2 *mm*) $= 62.50\eta_{\text{nom}} = 2.58L_{\text{nom}}$. Since the condition $\Delta/L_{\text{nom}} << 1$ is not satisfied, the modeled turbulence dissipation rate would significantly deviate from the true value, but may still be accurate enough to be used in industrial applications.

At other phase angles, as well as outside the vortex core even in the 0° and the 30° cases (but not in the immediate vicinity of the impeller blades), the turbulence level is smaller, and therefore the modeled dissipation rate would deviate from the true value by a smaller magnitude.

CONCLUSIONS

We worked out a mathematical expression for a low-pass filter (for energy spectrum) that ideally represents the spatial averaging effect that a PIV interrogation volume performs onto the true flow velocity field. This low-pass filter is the square of a *sinc* function, which is very different from the isotropic sharp cut filter which has been used till date to represent the PIV averaging effect. We used this low-pass filter together with a subgrid-stress model proposed by Meyers and Sagaut [19], in order to estimate the turbulence dissipation rate inside a stirred flow mixer. When we compared the dissipation rate directly calculated from the PIV measured velocity field inside the mixer with the modeled dissipation rate, we found the former to be underestimated by about 300 times. Note that the modeled dissipation rate is likely to contain some inaccuracy as well, because the interrogation volume size in the PIV measurement did not fall within the equilibrium range (in which the energy spectrum that is used in the subgrid-stress model is valid). Despite that, the modeled dissipation rate may still be used in industrial applications, because it estimates the true dissipation rate much more accurately than the otherwise hugely-underestimated, directly calculated dissipation rate.

REFERENCES

[1] Bachelor G. K., The theory of axisymmetric turbulence, *Proceedings of the Royal Society of London*, A 186, 1946, pp.480-502.

[2] Chandrasekhar S., The theory of axisymmetric turbulence, *Proceedings of the Royal Society of London*, A 242, 1950, pp.557-577.

[3] George W. K. and Hussein H. J., Locally axisymmetric turbulence, *Journal of Fluid Mechanics*, Vol. 233, 1991, pp.1-23.

[4] Scarano F., Tomographic PIV: principles and practice, *Measurement Science and Technology*, Vol.24, 2013, 012001 (28p).

[5] Shekhar C., Takahashi K., Matsunaga T., and Nishino K., Tomographic PIV measurement of turbulence characteristics and maximum shear stress in a square-shaped stirred flow mixer, *Proceedings of the 16th International Symposium on Flow Visualization, Okinawa, Japan*, June 2014.

[6] Shekhar C., Takahashi K., Matsunaga T., and Nishino K., Tomographic PIV measurement of turbulence energy budget equation terms in a square shaped stirred flow mixer, *Proceedings of the 17th International Symposium on Applications of Laser Techniques to Fluid Mechanics, Lisbon, Portugal,* July 2014.

[7] Bakker A, Myers K.J., Ward R.W., and Lee C.K., The laminar and turbulent flow pattern of a pitched blade turbine, *Transactions of IChemE*, Vol.74(A), 1996, pp.485-491.

[8] Ge C.Y., Wang J.J., Gu X.P., and Feng L.F., CFD simulation and PIV measurement of the flow field generated by modified pitched blade turbine impellers, *Chemical Engineering Research and Design*, Vol.92, 2014, pp.1027-1036.

[9] Khopkar A.R., Aubin J., Xuereb C., Sauze N.L., Bertrand J., and Ranade V.V. Gas-liquid flow generated by a pitched blade turbine: PIV measurements and CFD simulations, *Industrial & Engineering Chemistry Research,* Vol.42(21), 2003, pp.5318-5332.

[10] Delafosse A., Collignon M.L., Crine M., and Toye D., Estimation of the turbulent kinetic energy dissipation rate from 2D-PIV measurements in a vessel stirred by an axial Mixel TTP impeller, *Chemical Engineering Science*, Vol.66, 2011, pp.1728-1737.

[11] Alekseenko S.V., Dulin V.M., and Markovich., Stereo PIV measurements of fine-scale turbulence statistics in a free jet, *Proceedings of the 6th Symposium on Turbulence, Heat and Mass Transfer, Rome, Italy,* September 2009.

[12] Pope S.B., *Turbulent Flows*, Cambridge University Press, 2000.

[13] Smagorinsky J., General circulation experiments whith the premitive equations: I. The basic experiment, *Monthly Weather Review*, Vol.99, 1963, pp.99-165.

[14] Lilly D.K., The representation of small-scale turbulence in numerical simulation experiments, *Proceedings of IBM Scientific Computing Symposium on Environmental Sciences*, *IBM Data Processing Division, White Plains, New York*, 1967.

[15] Sheng J., Meng H., and Fox R.O., A large eddy PIV method for turbulence dissipation rate estimation, *Chemical Engineering Science*, Vol.55, 2000, pp.4423-4434.

[16] Shekhar C., Nishino K., Yamane Y., and Huang J., Stereo-PIV measurement of turbulence characteristics in a flow mixer, *Journal of Visualization*, Vol.15, 2012, pp.293-308.

[17] Alekseenko S.V., Bilsky A.V., Dulin V.M. and Markovich, D.M., Experimental study of an impinging jet with different swirl rates, *International Journal of Heat and Fluid Flow*, Vol.28, 2007, pp.1340-1359.

[18] Pao Y. H., Structure of turbulent velocity and scalar fields in large wave numbers, *Physics of Fluids*, Vol. 8, 1965, pp.163-175.

[19] Meyers J. and Sagaut P., On the model coefficients for the standard and the variational multi-scale Smagorinsky model, *Journal of Fluid Mechanics*, Vol. 569, 2006, pp.287-319.

[20] Willert C.E. and Gharib M., Digital particle image velocimetry, *Experiments in Fluids*, Vol.10, 1991, pp.181-193.

[21] Foucaut J.M., Carlier J., and Stanislas M., PIV optimization for the study of turbulent flow using spectral analysis, *Measurement Science and Technology*, Vol.15, 2004, pp.1046-1058.
[22] Foucaut J. M. and Stanislas M., Some considerations on the accuracy and frequency response of some derivative filters applied to particle image velocimetry vector fields, *Measurement Science and Technology*, Vol. 13, 2002, pp.1058-1071.
[23] The HR-100 impeller is manufactured by *Satake Chemical Equipment Limited, Japan* (http://satake.co.jp/English).
[24] Thompson W.R., On a criterion for the rejection of observations and the distribution of the ratio of deviation to sample standard deviation, *The Annals of Mathematical Statistics*, Vol.6(4), 1935, pp.214-219.
[25] Shekhar C., Nishino K., and Iso Y., Stereo-PIV measurement of shear stress in a stirred flow mixer, *Proceedings of the* 10th *International Symposium on Particle Image Velocimetry, Delft, The Netherlands*, July, 2013.
[26] Elsinga G.E., Scarano F., Wieneke B., and Oudheusden B.W., Tomographic particle image velocimetry, *Experiments in Fluids*, Vol.41, 2006, pp.933-947.

PROPER ORTHOGONAL DECOMPOSITION OF FLOW AROUND A LARGE MINING TRUCK

Sexton W. and Demuren A. *
*Author for correspondence
Department of Mechanical and Aerospace Engineering
Old Dominion University
Norfolk, Virginia, USA
E-mail: ademuren@odu.edu

ABSTRACT

Mining trucks usually operate in off-road situations in which environmental conditions are major impediments to efficiency. Tires raise dust from the un-tarred road, which pose health hazards for operators and could also clog up equipment, necessitating adequate spacing between trucks transporting mining load. Dust dispersion is largely affected by vortices generated by flow around truck bodies. The flow is complex, unsteady, turbulent, three-dimensional and asymmetric. Numerical simulation of the flow around a large mining truck requires several million grid nodes for adequate resolution. The many degrees-of-freedom required for the simulation makes is too computationally expensive for sensitivity analysis. Proper orthogonal decomposition (POD) is a post-processing technique for extracting the most energetic structures, thereby reducing the order required to reproduce the basic flow features. Detached eddy simulation of the flow around a mining truck is performed to generate the unsteady, three-dimensional flow field. For the present 3-D simulation, it was found, using POD, that the first 100 modes constitute more than 70% of the energy. These modes give good reproductions of the original transient velocity components and properties such as Reynolds stresses derived therefrom. The reconstituted velocity field represents a reduced order model of the true flow field, which can subsequently be used for sensitivity analysis.

INTRODUCTION

Direct simulation of turbulent flows requires computational effort, which is related to higher powers of the Reynolds number, Re. If N is the number of degrees of freedom needed to resolve all facets of the flow, then it has been shown that N is of order $Re^{9/4}$, for three-dimensional turbulent flows (Launder et al 1984). For practical flows, a reduction in effort is required. The ultimate approach is to perform an *a-priori* time-average of the equations, which filters out all small and large scales, while replacing their effects with an enhanced mixing coefficient called the eddy viscosity. In the process, important dynamics of the flow physics is lost, especially in vortex dominated rather than shear dominated flows. Turbulent flows around bluff bodies belong in this category. To capture important dynamics, large eddy simulation (LES) may be performed in which only the small scales are filtered out. Although there is considerable reduction in order, which makes LES a practical tool (Rodi et al 1997), it remains a computationally intensive method, not suitable for engineering design or sensitivity analysis. A somewhat computationally less demanding variant is the detached eddy simulation (DES), which works well for bluff-body flows (Spalart 2009). A promising method of reduced-order-modeling, which preserves the most important coherent structures is based on proper orthogonal decomposition (POD). Holmes et al. (1996, 1997), Smith et al. (2005) showed that salient features of turbulent flows may be captured by extracting the most energetic structures. In the POD method an eigen-system equation is formulated, which when applied to two-point velocity correlation tensors derived from the velocity field enables the mode shapes of the most energetic structures to be extracted. By concentrating the application of POD to the fluctuating velocity components, a selection of the highest ranked energies and modes from the POD can reconstruct turbulent flow parameters such as Reynolds Stress and kinetic energy with reasonable accuracy compared to the original flow field. Successful application of POD (Reichert et al. 1994, Gunzberger and Wilcox 2005), by ranking the most energetic structures, results in significant reduction in the number of degrees of freedom required to characterize and reproduce the turbulent flow.

MATHEMATICAL FORMULATION – PROPER ORTHOGONAL DECOMPOSITION

In the POD method, the eigen-system mathematically represents the energies by the eigenvalues, λ^m, and corresponding modes (or turbulent coherent structures) by the eigenvectors, $\Phi_{i,m}$; where "i" is the node number and "m" is the mode number (highest energy at m = 1). The eigen-system equation is in the form $A\Phi_{j,m} = \lambda^m\Phi_{i,m}$; where A is a square matrix that contains flow characteristic information about each point in the domain. Holmes et al. (1996) showed that both the ranked energies and square characteristic matrix evolve together, by optimizing the maximum energy, written as:

$$\max_{\Phi \in L^2([0,1])} \frac{\left\langle \left|(u,\Phi)\right|^2 \right\rangle}{\left\|\Phi\right\|^2} \qquad (1)$$

Brackets, < * >, expresses an ensemble average, brackets, | * |, signifies a modulus, and brackets, || * ||, indicate the L^2-norm. $L^2([0,1])$ is a infinite-dimensional Hilbert space of a square integrable function. The inner product (u,Φ) is the square integrable function; which can be written as:

$$(f,g) = \int_0^1 f(X)g^*(X)\,dX \qquad (2)$$

Similarly:

$$\left\|f(X)\right\|^2 = \left(f,f\right) = \int \left|f(X)\right|^2 dX \qquad (3)$$

This inner product function formed the basis for the square characteristic matrix. In Eq. (1) the maximization constraint is $\|\Phi\|^2 = 1$. Following Holmes et al. (1996), it can be shown that the fundamental basis of the eigen-system reduces to:

$$\int_0^1 \left\langle u(X)u^*(X') \right\rangle \Phi(X')\,dX' = \lambda\Phi(X) \qquad (4)$$

where X and X′ are at different locations in the domain. Thus, $u(X)u^*(X')$ is a square correlation matrix of velocities, obtained by DES in the present study, throughout the whole domain, which is a two-point correlation tensor, R_{ij},

$$R_{ij}\left(X,X'\right) = \left\langle u(X)u^*(X') \right\rangle \equiv \overline{u_i(X)u_j(X')} \qquad (5)$$

Thus,

$$\int_\Omega R_{ij}(X,X')\Phi_{j,m}(X')\,dX' = \lambda^m\Phi_{i,m}(X) \qquad (6)$$

which is in the eigen-system form, $A\Phi_{j,m} = \lambda^m\Phi_{i,m}$, where square matrix A is R_{ij} is ultimately what the POD method mathematically had been working to achieve; that is $R_{ij}\Phi_{j,m} = \lambda^m\Phi_{I,m}$. The challenge of Eq. (6) is to solve the integral eigen-system numerically. Following Reichert et al. (1994), a diagonal matrix, **D**, is formed that contains quadrature weights that are products of Δd (incremental distances, i.e., Δx, Δy, or Δz) and trapezoidal-rule integration weights, 0.5,1,1,…,1,1,0.5 for n locations (Ramsay and Silverman, 1997). However, it proved beneficial for the numerical integration to have the uniform incremental distances for each direction. So, the numerical version of Eq. (6) takes the new form,

$$\mathbf{RD}\Phi = \lambda\Phi \qquad (7)$$

Reichert et al. (1994) stated that **R** loses its symmetry when it is post-multiplied by **D**. Therefore, the following manipulations are performed to retain symmetry in the eigen-system form. Where, **RD** from the Eq. (7) becomes $\sqrt{\mathbf{D}}\,\mathbf{R}\sqrt{\mathbf{D}}$, the energies remain, λ, and the modes, Φ, are found by Ψ divided by $\sqrt{\mathbf{D}}$.

$$\mathbf{R}\sqrt{\mathbf{D}}\sqrt{\mathbf{D}}\Phi=\lambda\Phi$$

$$\Psi=\sqrt{\mathbf{D}}\Phi$$

$$\mathbf{R}\sqrt{\mathbf{D}}\Psi=\lambda\Phi$$

$$\sqrt{\mathbf{D}}(\mathbf{R}\sqrt{\mathbf{D}}\Psi=\lambda\Phi)$$

$$\sqrt{\mathbf{D}}\,\mathbf{R}\sqrt{\mathbf{D}}\Psi=\lambda\Psi \tag{8}$$

The last step in the POD process is to create the random modal coefficients, a^m. This was done using Einstein's summation rule, i = 1 to 3, in:

$$a^m = \int u_i(X)\Phi_{i,m}(X)dX \tag{9}$$

Now, the three essential parts, $\Phi_{i,m}$, λ^m, and a^m, to the POD have been obtained. The POD eigen-system is solved with the MATLAB software. If it is completed properly there are a few properties that can be checked to validate the results. These are:

1) Numerical error determined by $\mathbf{RD}\Phi - \lambda\Phi = 0$

2) Modal orthonormality:

$$\int \Phi_i^n(X)\Phi_i^m(X)dX = \delta_{nm} \tag{10}$$

$$\delta_{nm} = \begin{matrix} 1; n = m \\ 0; n \neq m \end{matrix}$$

Numerically this in matrix form will result in an Identity,

$$\mathrm{inv}(\Psi)\ \Psi = I \tag{11}$$

Or,

$$\mathrm{inv}(\Phi)D\Phi = I \tag{12}$$

3) $\lambda \propto a$

$$\overline{a^n a^m} = \lambda^n \delta_{nm} \tag{13}$$

4) Total Energy (Reichert et al., 1994),

(integral)

(numerical)

$$E_{TOT} = \int \overline{u_i(X)u_i(X)}dX = \int R_{ii}dX \tag{14}$$

$$E_{TOT} = \sum diag(R_{ii}D) \tag{15}$$

$$E_{TOT} = \sum_{m=1}^{M} \lambda^m \tag{16}$$

Furthermore, any flow property that is a function of velocity can be reconstructed from $\Phi_{i,m}$, λ^m, and a^m, namely:

1) Instantaneous fluctuating velocity field

$$u_i(X) = \sum_{m=1}^{M} a^m \Phi_{i,m}(X) \tag{17}$$

2) Reynolds stress

$$\overline{u_i(X)u_j(X)} = \sum_{m=1}^{M} \lambda^m \Phi_{i,m}(X)\Phi_{j,m}(X) \tag{18}$$

3) Kinetic energy

$$\frac{1}{2}\overline{u_i(X)u_i(X)} = \frac{1}{2}\sum_{n=1}^{N} \lambda^n \left[\Phi_i^n\right]^2 \tag{19}$$

No single mode can individually represent the complete turbulent flow behavior. However, with some manipulations of POD eigen-system results, $\Phi_{i,m}$, λ^m, and a^m, flow-field reconstruction will steadily become more accurate with continual addition of modes. Energies and modes are unique to a given problem; a set number of modes for one model may not give as good a representation as on another. Resoundingly, POD is a successful means of capturing the majority of the turbulent energies in a significantly truncated form while the flow-field reconstruction remains extremely accurate. Therefore, this is a viable method for ROM in complex turbulent flows.

APPLICATION TO LARGE MINING TRUCK

Figure 1 shows a picture of a 1:30 scaled model of a large mining truck. The full-scale truck has an overall length of 14.5m, height of 7.6m and width of 9.8m. The model used in this research was scaled at 1:30 (0.033). The scaled model measured 0.484m long, 0.275m tall and 0.325m wide. The overall computational domain size was 5-truck lengths long (2.431m), 3-truck heights tall (0.849m), and 5-truck widths wide (1.632m). In the computational domain the model was set back 1-truck length from the inlet-face (3-truck lengths behind), centered spanwise (2-truck widths on each side) and positioned at the bottom of the domain (2-truck heights above). A detached eddy simulation was performed, using a combination of tetrahedral and hexagonal meshes. Uniform hexagonal meshes were used in the data collection planes in the rear of the truck, show in Fig. 1. Total cell count was 15.3 million, with 4.3 million nodes. There were 21,658 mesh cells in each data collection plane.

For a complete reconstruction of a velocity field, an infinite number of energies and modes are needed. In the POD process, the maximum number of energies and modes that can be obtained is the number of grid points times the number of velocity components. For the DES, the POD could find a maximum of 65,280 energies and corresponding modes (170 x 128 times 3 velocity components). It was found that during the POD process, that on average, about 72% of the total energy was contained within the first 100 modes. The total energy was found by the sum of the diagonal components of the double-integrated two-point correlation matrix ($\Sigma\iint R_{ii}$) and the sum of the eigenvalues. Table 1 shows the results of the validity test of the POD results. The error in the difference of the left-hand side and right-hand side of the eigen-system was found to be on the order of machine zero (10^{-17}) and identities were confirmed in the orthogonality test of the eigenvectors. The total energy ($\Sigma\iint R_{ii}$) and the sum of the eigenvalues ($\Sigma\lambda$) for the first 100 modes for each plane are shown.

Table 2 shows the breakdown of energy and percent of $\Sigma\lambda$ energy per POD mode for each plane, for the first 20 modes. For the driver plane, the modal energy fell below 1% of the total energy by mode 20, which equated to ~53% of $\Sigma\lambda$ energy and ~38% of the total energy. 50% and 60% of the total energy were found up to modes 37 and 58, respectively. The modal energy fell below 1% of the total energy by mode 19 in the mid plane, or ~50% of $\Sigma\lambda$ energy and ~35% of the total energy. 50% and 60% of the total energy are found up to modes 40 and 62, respectively. In the passenger plane, the modal energy fell below 1% of the total energy by mode 20, which equated to ~52% of $\Sigma\lambda$ energy and ~38% of the total energy. 50% and 60% of the total energy are found up to modes 37 and 57, respectively.

Table 1. Validity Tests of DES – POD matrices

	Driver	Mid	Pass
$R\Psi - \Psi\lambda = 0$ (~ 10^{-17}) (matrix maximum value)	2.89	3.73	3.34
$(inv(\Psi))(\Psi) = I$ (diagonal components)	1	1	1
$(inv(\Phi))D(\Phi) = I$ (diagonal components)	1	1	1
E_{tot} ($\Sigma\iint R_{ii}$)	2.68	2.22	3.07
E_{tot} ($\Sigma\lambda$)	1.93	1.58	2.22
% of E_{tot} of $\Sigma\lambda$ (1^{st} 100 modes)	72%	71%	73%

Table 2. DES – POD Energies for the first 20 modes: (A) Modal Energy, (B) Cumulative Energy, (C) % of Eigenvalue Energy, (D) % of Total Energy

	Driver Plane				Mid Plane				Pass Plane			
modes	(A)	(B)	(C)	(D)	(A)	(B)	(C)	(D)	(A)	(B)	(C)	(D)
1	0.109	0.109	5.64%	4.07%	0.079	0.079	5.02%	3.58%	0.122	0.122	5.50%	3.99%
2	0.105	0.214	11.08%	8.00%	0.066	0.146	9.22%	6.57%	0.113	0.235	10.58%	7.67%
3	0.090	0.304	15.76%	11.38%	0.062	0.208	13.14%	9.37%	0.097	0.333	14.95%	10.84%
4	0.086	0.391	20.23%	14.61%	0.059	0.266	16.85%	12.01%	0.085	0.417	18.76%	13.60%
5	0.067	0.458	23.71%	17.12%	0.055	0.321	20.34%	14.50%	0.078	0.496	22.29%	16.15%
6	0.057	0.515	26.68%	19.27%	0.051	0.372	23.56%	16.80%	0.062	0.558	25.08%	18.18%
7	0.053	0.569	29.44%	21.26%	0.047	0.419	26.55%	18.93%	0.060	0.617	27.76%	20.12%
8	0.048	0.617	31.94%	23.07%	0.042	0.461	29.22%	20.83%	0.058	0.675	30.37%	22.01%
9	0.045	0.662	34.26%	24.74%	0.040	0.501	31.73%	22.62%	0.056	0.731	32.87%	23.82%
10	0.043	0.703	36.48%	26.35%	0.036	0.537	33.99%	24.23%	0.053	0.784	35.25%	25.54%
11	0.039	0.744	38.52%	27.82%	0.035	0.572	36.21%	25.81%	0.047	0.831	37.35%	27.07%
12	0.038	0.782	40.49%	29.25%	0.032	0.603	38.21%	27.24%	0.044	0.874	39.32%	28.49%
13	0.036	0.819	42.37%	30.60%	0.031	0.634	40.16%	28.63%	0.042	0.916	41.19%	29.85%
14	0.034	0.852	44.12%	31.86%	0.030	0.664	42.05%	29.98%	0.039	0.955	42.95%	31.13%
15	0.032	0.885	45.79%	33.07%	0.028	0.692	43.80%	31.22%	0.038	0.993	44.67%	32.37%
16	0.031	0.915	47.37%	34.21%	0.024	0.716	45.33%	32.31%	0.036	1.029	46.30%	33.55%
17	0.030	0.945	48.92%	35.33%	0.024	0.740	46.84%	33.39%	0.034	1.064	47.83%	34.66%
18	0.028	0.973	50.34%	36.36%	0.022	0.762	48.26%	34.40%	0.033	1.097	49.31%	35.73%
19	0.026	0.999	51.69%	37.33%	0.022	0.78	49.62%	35.37%	0.032	1.128	50.73%	36.76%
20	0.025	1.024	53.00%	38.28%	0.021	0.805	50.97%	36.33%	0.031	1.159	52.11%	37.76%

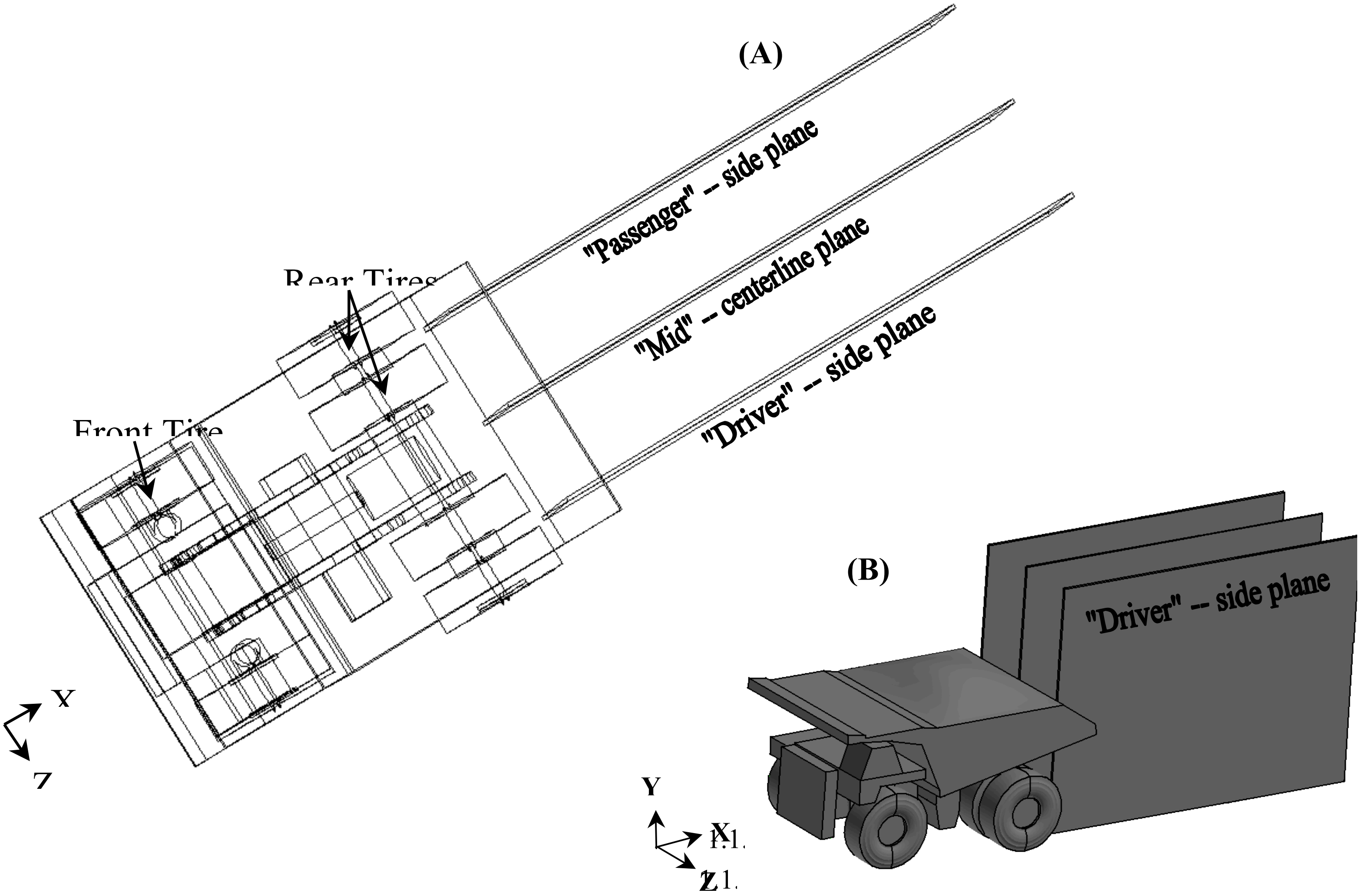

Figure 1: Mining truck model: (A) Top View; (B) Perspective; showing data collection planes on the rear.

The POD separates and orders modal energies in each of the X, Y, and Z direction for the given area. Figure 2 shows a selection of POD modes for each plane. The trailing end of the dump bed is outlined between X/L = 0 and 0.1 and Y/L = 0.34 and 0.47. The figure is defined by $\Phi_{i,m}$, where "i" is the direction and "m" is the mode number. For example purposes, only the streamwise and normal modal directions (i = X) and modes (m =) 1, 30, and 100 were selected and shown in these figures. These figures display the large turbulent behavior, which are low frequencies (fewer numbers) but contain high energies descending to the small turbulent behaviors which have high frequencies (numerous) but contain less energy. Many behaviors in these figures are seen in the contours of the DES. The flow on the driver and passenger planes is nearly parallel to the road surface in modal structures. Likewise in mid plane, the affects of the airflow under the truck chassis can be seen in the low modal structures.

PROPER ORTHOGONAL DECOMPOSITION RECONSTRUCTION

POD has been demonstrated that it is able to separate the energies and structures of turbulent flow (in this application) for detailed study. The other significant benefit is the reduction of the data set and recreation of the original data set from the truncated one. Sample reconstructions of fluctuating streamwise velocity field for the driver plane is shown in Fig. 3. The figure has the velocity field from the original data set compared to reconstructions from the first 20, 50, and 100 modes. The reconstructions in these figures were developed from Eq. (20), which is the fluctuating velocity field reconstruction equation shown by Reichert et al. (1994). This equation is the sum of the product of the random POD coefficient (a^m) and the modal shape ($\Phi_{i,m}$).

$$u_i(X) = \sum_{m=1}^{M} a^m \Phi_{i,m}(X) \tag{20}$$

Visually from the figure, it is clear that added modes included in the reconstruction provide a better representation. By examining of a correlation coefficient and its coefficient of determination between the original data set and each reconstruction, one can gauge the accuracy of the representation. Bloom (2009) defined the correlation coefficient (r) by Eq. (21) (also known as the Pearson product moment correlation coefficient).

$$r = \frac{n\sum xy - \left(\sum x\right)\left(\sum y\right)}{\sqrt{n\left(\sum x^2\right) - \left(\sum x\right)^2}\sqrt{n\left(\sum y^2\right) - \left(\sum y\right)^2}} \tag{21}$$

Where "x" and "y", for this work would be the original data set matrix and reconstruction matrix and "n" is the number of points in the plane. Bloom (2009) stated that as r→±1, the correlation is strong. However, she showed that by calculating the coefficient of determination (R^2), Eq. (22), one can gauge what percentage of the correlation is actually a linear relation between, in this case, the data set and the reconstruction with the remaining percentage related to random influences.

$$R^2 = r^2 \tag{22}$$

Table 3 shows the correlation coefficients and percent coefficient of determination for the reconstructions of streamwise and road-normal velocity fluctuations of the three planes. Not surprisingly, the reconstructions with only 20 modes provided the lowest correlation at 0.62 and a coefficient of determination at 38% linear relation (or 62% random influences). The best correlation coefficient found was 0.97 with 94% coefficient of determination (or 6% random influences) for reconstructions with 100 modes.

Table 3. Correlation Coefficient (r) and Coefficient of Determination (%R^2) for POD reconstruction of velocity fluctuations' contours for each plane

	Driver Plane				**Mid Plane**				**Passenger Plane**			
	u'		v'		u'		v'		u'		v'	
Modes	r	R^2	r	R^2	r	R^2	r	R^2	r	R^2	r	R^2
20	0.753	56.7%	0.756	57.2%	0.698	48.8%	0.713	50.9%	0.752	56.6%	0.619	38.3%
50	0.901	81.2%	0.897	80.5%	0.872	76.1%	0.928	86.1%	0.935	87.3%	0.868	75.3%
100	0.953	90.8%	0.950	90.2%	0.957	91.6%	0.968	93.7%	0.964	93.0%	0.933	87.1%

CONCLUSION:

POD has been demonstrated to be an efficient reduced-order model for the wake flow behind a scaled mining truck. More than 70% of the energy is contained in the first 100 modes. POD modal energy fell below 1% of the total energy up to mode 21, which equated to ~50% of Σλ energy and ~35% of the total energy. Modes at 50% and 60% of the total energy were found up 40 and 62, respectively. These modes are used to successfully reconstruct the velocity field and Reynolds stresses.

REFERENCES

1. Bloom, R. 2009. "Linear Regression and Correlation: The Correlation Coefficient and Coefficient of Determination (modified R. Bloom)." *Connexions*, December 23, 2009.

2. Gunzburger, M. K. Wilcox. 2005. "Reduced-Order Models of Large-Scale Computational Systems." Society for Industrial and Applied Mathematics, June 10, 2005

3. Holmes, P., Lumley, J. L. and Berkooz, G. eds. 1996. Turbulence, Coherent Structures, Dynamical Systems, and Symmetry. New York: Cambridge University Press.
4. Holmes, P. J., Lumely, J. L., Berkooz, G., Mattingly, J. C. and R. W. Wittenberg. 1997. "Low-Dimensional Models of Coherent Structures in Turbulence." Physics Reports 287:337-384
5. Launder, B.E., Reynolds, W.C., Rodi, W., Mathieu, J., Jeandel, D., 1984 *Turbulence models and their applications,* Editions Eyrolles, Paris.
6. Ramsay, J. O. and B. W. Silverman, eds. 1997. *Functional Data Analysis*. New York: Springer.
7. Reichert, R. S., Hatay, F. F., Biringen, S. Huser. A. 1994. "Proper orthogonal decomposition applied to turbulent flow in a square-duct." Physics of Fluids 6(9).
8. Rodi, W. Ferziger, J.H. Breuer M. and Pourquiée M., 1997, Status of Large Eddy Simulation: Results of a Workshop, J. Fluids Eng. 119(2), 248-262.
9. Smith, T. R., Moehlis, J. and Holmes. P. 2005. "Low-Dimensional Modeling of Turbulence Using The Proper Orthogonal Decomposition: A Tutorial." Nonlinear Dynamics 41:275-307.
10. Spalart, P.R., 2009 Detached eddy simulation, Annual Review of Fluid Mech., 41, 181-202.

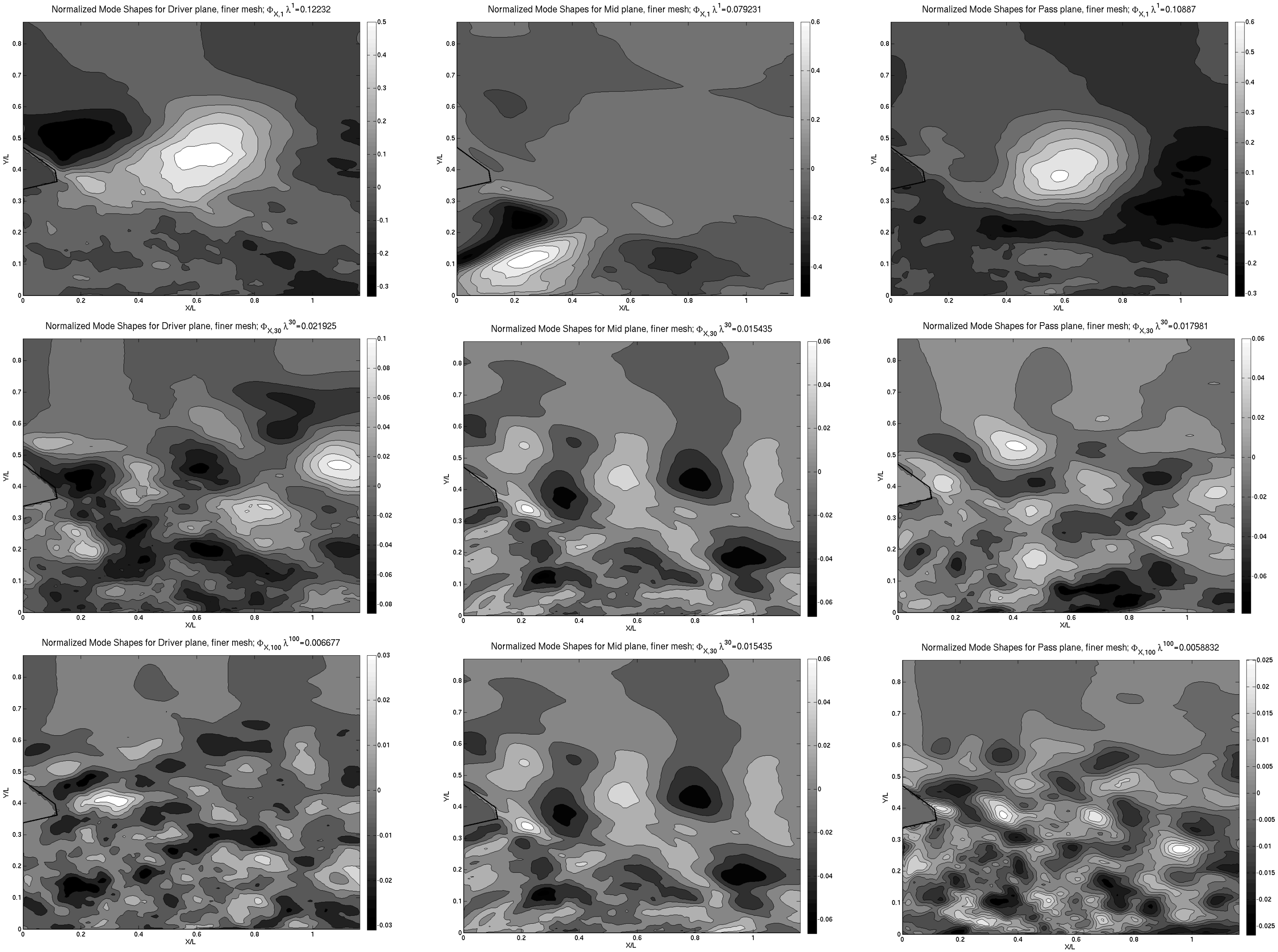

Normalized Mode Shapes for Driver plane, finer mesh; $\Phi_{X,1}$ λ^{1}=0.12232

Normalized Mode Shapes for Mid plane, finer mesh; $\Phi_{X,1}$ λ^{1}=0.079231

Normalized Mode Shapes for Pass plane, finer mesh; $\Phi_{X,1}$ λ^{1}=0.10887

Normalized Mode Shapes for Driver plane, finer mesh; $\Phi_{X,30}$ λ^{30}=0.021925

Normalized Mode Shapes for Mid plane, finer mesh; $\Phi_{X,30}$ λ^{30}=0.015435

Normalized Mode Shapes for Pass plane, finer mesh; $\Phi_{X,30}$ λ^{30}=0.017981

Normalized Mode Shapes for Driver plane, finer mesh; $\Phi_{X,100}$ λ^{100}=0.006677

Normalized Mode Shapes for Mid plane, finer mesh; $\Phi_{X,30}$ λ^{30}=0.015435

Normalized Mode Shapes for Pass plane, finer mesh; $\Phi_{X,100}$ λ^{100}=0.0058832

Figure 2. DES – POD normalized streamwise modal shapes ($\Phi_{X,m}$) for modes m = 1, 30, 100; (top to bottom; Driver Plane – left column, Mid Plane – middle column, Passenger Plane – right column)

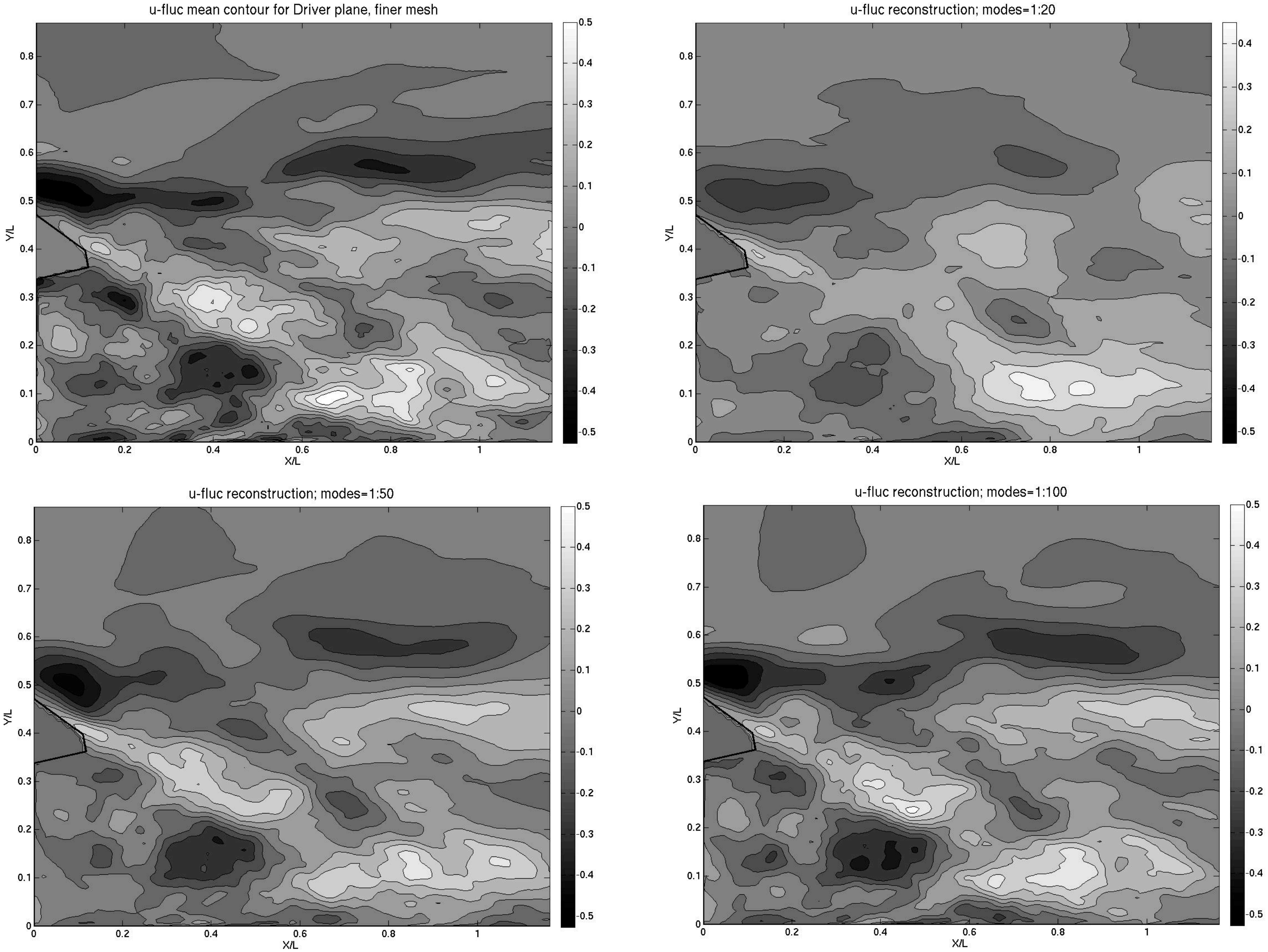

Figure 3. Original streamwise fluctuating velocity field data set contour and 1:20 modes, 1:50 modes, and 1:100 modes DES POD reconstructions for the Driver Plane

CHARACTERISATION OF SECOND GENERATION ALTERNATIVE DIESEL FUEL SPRAYS

Dragomirov P.*, Sauerhering J., Beyrau F. and Schmidt J.
*Author for correspondence
Institute of Fluid Dynamics and Thermodynamics,
Otto von Guericke University of Magdeburg,
Magdeburg, 39106,
Germany,
E-mail: plamen.dragomirov@ovgu.de

ABSTRACT

This work contributes to the analysis and characterisation of alternative Diesel fuels. High speed visualisation techniques and phase Doppler anemometry (PDA) were used in order to investigate the fuel atomisation and air-fuel mixing properties of several alternative fuels and compare them to conventional Diesel fuel. One of the selected alternative fuels is derived through a Fischer-Tropsch synthesis of natural gas (FT), where the other two are second generation bio fuels BF1 and BF2. For the fuel characterisation a continuously purged pressure chamber was employed in order to simulate engine like conditions and to investigate the impact of different operating conditions on fuel atomisation and evaporation.

Slightly smaller droplet diameters and increased spray angles were observed in the case of FT and BF2 compared to the standard Diesel. However the investigations shows that the alternative fuels have comparable air-fuel mixing properties to the Diesel fuel. Nevertheless the combustion process and the resulting exhaust emissions are not governed only by spray characteristics of the fuels. The chemical properties play a crucial role in the combustion and preliminary combustion visualisations show that these also need to be thoroughly investigated in a future work as shown by some initial combustion visualisations of BF2 and Diesel fuel in optical engine.

INTRODUCTION

Vehicle propulsion relies heavily on the combustion of fossil fuels as an energy source, which results in unwanted pollutant emissions of particulate matter, CO_2, NO_x and others. In order to reduce these harmful emissions, new vehicles must adhere to ever stricter exhaust emission standards. To fulfil these standards, the continuous improvement of the internal combustion engine is necessary. However the future energy scenarios suggest that due to ever increasing crude oil prices, the further improvement of the fossil fuel combustion may not suffice and that the use of renewable alternative fuels as well as electro mobility will play an important role. However the electro mobility still has disadvantages such as battery problems and range. For this reason many range-extender concepts e.g. the range-extender under the public project COMO[1], exist to compensate the short range of electric vehicles, which also gives the opportunity to utilise alternative diesel. Therefore first and second generation bio-fuels are becoming more and more the focus of scientific investigations. However, despite the big interest in alternative Diesel fuels over the years, the influence of the divergent fuel properties, e.g. density, viscosity and others, on the process of atomization, ignition, combustion and emission production is still not resolved.

Therefore the scope of the current study involves the analysis and characterisation of such alternative Diesel fuels using high speed visualisation and phase Doppler anemometry. In order to characterise the fuels at conditions relevant for the range-extender concept a continuously purged pressure chamber was employed.

NOMENCLATURE

CA	[°]	Crank angle
d_s	[mm]	Spray diameter
l_p	[mm]	Pixel length
P	[mm]	Penetration
P_{Air}	[bar]	Air pressure
P_{Inj}	[bar]	Injection pressure
t	[ms]	Time
T_{Air}	[K]	Air temperature
TDC		Top dead centre
V	[mm^3]	Volume

EXPERIMENTAL SETUP AND EQUIPMENT

For the investigation of the spray characteristics of the fuels of interest a high pressure vessel was employed to reproduce engine-like conditions.

High pressure chamber and fuel injection system

The pressure chamber has two by two opposite facing openings with a diameter of 80 mm. In order to provide good measurement conditions for the employed Phase Doppler Particle Analyser (PDPA) system one of them is shifted 20° with respect to the opposite, see Figure 1. Three openings were fitted with silica glass windows and the fourth was used to

---

[1] Competence in Mobility (COMO) funded by the Land Sachsen Anhalt and the European Commission

mount the diesel injector. For this purpose an adaptation of the injector holder introduced in [1] was employed, see Figure 1. Cooling fluid runs through the injector holder in order to keep the injector temperature constant. To avoid fuel accumulation the pressure chamber is vertically purged, where the air velocities are negligible in comparison to the spray velocities. Prior to entering the chamber the airflow passes through a heating system. More information about the specifications of the pressure chamber can be found in Table 1.

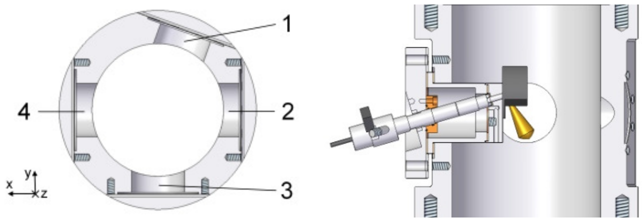

Figure 1 horizontal cross-section of the pressure chamber (left) and the injector mounted with the holder (right)

Table 1 Pressure chamber specifications

Length	412	mm
Diameter	200	mm
Max. pressure	60	bar
Max. temperature	400	°C

For the current investigations a common rail injection systems with a solenoid-driven injector with an 8 hole nozzle was used, see specifications in Table 2. The injection system was operated by a freely-adjustable control unit.

Table 2 Injection system specifications

Fuel injection system	Common rail, Bosch
Pump	CP3, Bosch
Injector actuation	Solenoid, Bosch
Nozzle type	Nano-sac-hole
Nozzle hole number	8
Diameter of the orifice	107 µm
Inclination angle of the orifice	81.7°

The investigations via high-speed imaging and phase Doppler anemometry (PDA) were focused on single spray, the central fuel jet pointing downwards. This way the spray of interest can be better resolved, which would increase the measurement precision. However the atomisation investigations are highly dependent on the measurement conditions requiring clean paths for the laser beams and the scattered light. Some of the sprays are directed towards the windows leading to fuel deposition. Moreover the adjacent fuel jets of the currently investigated spray would obstruct the laser beams and block the side view to this spray. Therefore a separation device was developed to deflect the neighbouring fuel jets from the field of view, see schematics in Figure 2. Similar approaches to isolate one spray were shown in [2-4]. The functionality of the separation device was tested at different injection pressures and timings and no influence of the separation device on the fuel spray was noticeable, see an example in Figure 2.

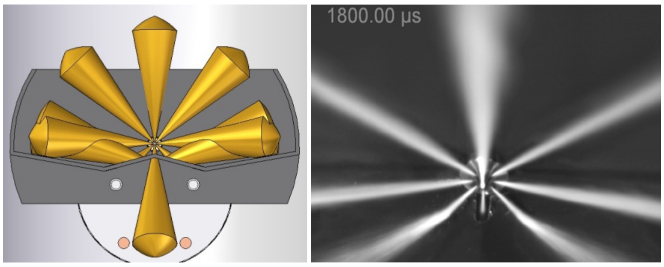

Figure 2 Separation device: schematic diagram (left) and raw image indicating its functionality (right)

Mie-scattering technique

In order to obtain information about the spray geometry the fuel jets were visualised with a *LaVision* high speed camera, see specifications in Table 3. As an illumination source a LED panel consisting of 16 high power LEDs with a combined output power of about 1.5 kW was used. The light source was positioned in front of the 70 ° window and the camera provided side view of the spray, see schematics in Figure 3. The scattered light from the fuel droplets was collected with an 85 mm wide-aperture Carl Zeiss lens, see specifications in Table 3. The spray propagation was investigated at a frame rate of 20 kHz which limited the image resolution to 1024 by 288 pixels. The image exposure time was set to 9 µs in order to freeze the flow motion.

Table 3 Specifications of the high speed system

HighSpeedStar 6 (HSS6)		**Carl Zeiss**	
Pixel size	20 x 20 µm	Type	PlanarT*
Resolution	1024 x 1024	Focal length	85 mm
Pixel depth	12 bit	Aperture range	1.4-16
Max. frame rate	650 kHz	Focus range	1 m - ∞
Min. Exposure time	< 1 µs		

For the geometrical spray analysis the commercial software DaVis was used, which enables the estimation of the spray cone angle and penetration. After a dark image subtraction a 5% threshold from the maximal image intensity was used to detect the spray. For the estimation of the spray penetration the "count min" mode from LaVision's geometry package was used, where a minimal distance from the nozzle (8 mm) and percentage of the spray pixels included in the penetration calculation (99%) can be defined. Thereby the first 8 mm that are obscured by the separation device can be excluded from the calculations. The cone angle was estimated with the "count max" mode, where the software starts with a small angle and opens it slowly until a given percentage (95% in the current work) of the spray falls into to the area formed by the measured angle. This mode enables the determination of minimal and maximal distances from the nozzle tip, respectively 8 and 20 mm in this work, which define the spray area to be considered for the angle calculations.

In order to calculate the spray volume the spray diameter was estimated at all pixel columns along the spray penetration. Then using the following equation all small cylindrical volumes with a length of one pixel and the corresponding diameter were summed up.

$$V(t) = \frac{\pi}{4} l_p \sum_{j=1}^{P(t)/l_p} d_{s,j}^2 \qquad (1)$$

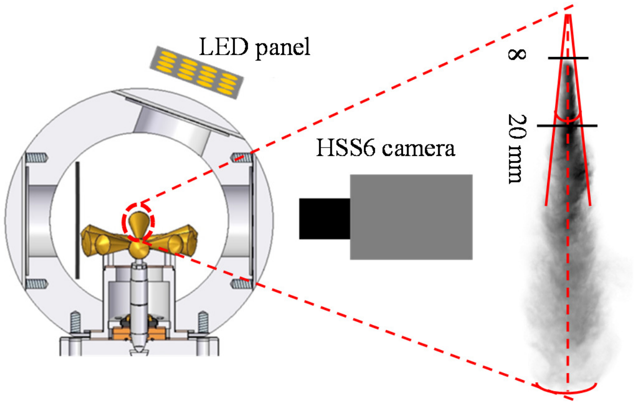

Figure 3 Experimental setup for high speed visualisation (left) and geometry analysis (right)

Phase Doppler anemometry

To investigate the atomisation characteristics of the fuels of interest a "High Dense 2D-PDPA system" from *Dantec* was used. The phase-Doppler technique for simultaneous detection of the velocity and size of transmitting and refracting particles was first-introduced by Zhao and Durst [5] in 1975 and has become a standard instrument for spray characterisation e.g. [6, 7]. Therefore the measurement principal will not be addressed in this work, and for details the reader is referred to[8].

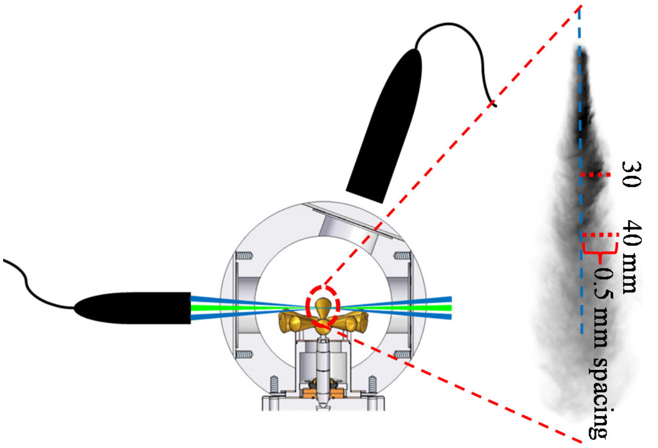

Figure 4 Experimental setup for PDA (left) and measurement points in the spray (right)

In order to detect scattered light of first refraction order, the receiving optic was positioned at a 70 ° angle, see schematics in Figure 4. This scattering angle is near the Brewster angle, where the droplet diameter estimation is relatively insensitive to the refraction index of the fuel [9]. More information about the system specifications is listed in Table 4.

Table 4 2D-PDPA system specifications

Focal length	310 mm
Aperture	80 mm
Slit	100 µm
Scattering angle	70 °
Diameter of the measurement volume	47 µm

To obtain representative information about the spray atomisation measurements on multiple positions in the spray were performed. The measurement positions in this work were chosen to have optimised measurement conditions in regions of the sprays that are significant for real engines. Near the nozzle hole the spray is very dense and there is a high probability for ligaments and thereby non-spherical particles to pass through the measurement volume and as a result no reliable measurements can be performed in this region. Therefore the fuel jets were investigated at 30 and 40 mm axial distances from the nozzle hole, where the radial position was varied from the spray centre with a 0.5 mm spacing, see Figure 4.

Operating conditions and investigated fuels

Three second generation alternative fuels were selected to analyse their spray characteristics and compare them with conventional Diesel fuel (Ref) as a reference fuel. One of them is derived through a Fischer-Tropsch synthesis of natural gas (FT) and the other two are biogenic fuels (BF1 and BF2). The second generation alternative fuels chosen for analysis in this study are made to resemble the Diesel fuel in order to be easily implemented in modern diesel engines. As a result their physical properties are very similar. Some of the fuel properties are shown in Table 5, in relation to reference fuel.

Table 5 Fuel properties relative to the reference fuel

Property	**Ref**	**FT**	**BF1**	**BF2**
Density (15°C)	-	↓	↓	↓
Viscosity (40°C)	-	↓	↑	↑
Surface tension	-	↓	↓	↓

To investigate the fuels and the influence of different operating parameters two operating points from the range extender were selected. However the temperatures during the main injection are significantly higher than the maximal temperature for the pressure chamber. Therefore to have comparable conditions the air density in the cylinder as a main parameter influencing the atomisation was chosen as a referencing parameter. Then the necessary air pressure was calculated in order have the same density in the pressure chamber at 50 and 150 °C air temperatures. All operating points are listed in Table 6.

Table 6 Operating points

	Air density [kg/m³]	Temperature [°C]	Injection pressure [bar]
1	18.1	50	600
2	18.1	50	1600
3	18.1	150	600
4	18.1	150	1600
5	41.1	50	600
6	41.1	50	1600
7	41.1	150	600
8	41.1	150	1600

RESULTS AND DISCUSSION

In order to get more reliable and representative trends statistical test evaluation was applied, which was first-introduced in [10] and is now a well-established statistical evaluation method [11, 12]. For the analysis the statistical software Visual-Xsel was used. A mean value representing all radial measurement positions at 40 mm distance was used for the evaluation of the Sauter mean diameter (SMD) and mean diameter. In the case of the spray geometry, the angle, penetration and volume were introduced as a function of the time after the start of injector energising. The results will be shown for discussion in this section in the form of graphs representing the effects of the different system inputs on the measured values and the dotted lines show the averaged value of the investigated parameter of the fuels.

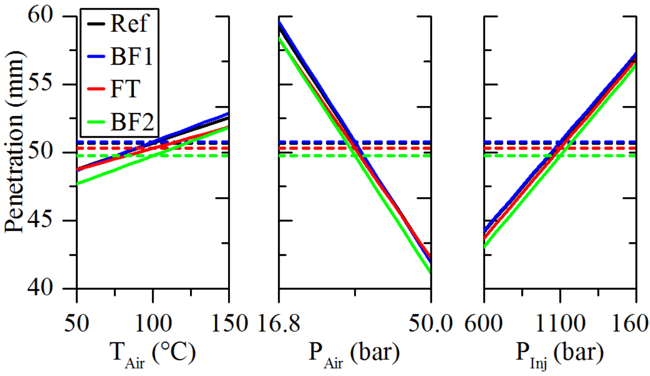

Figure 5 Effect of the operating parameters on the spray penetration for all fuels

Figure 5 shows the dependence of the spray penetration on the investigated parameters for all fuels. With increasing injection pressure, a longer spray penetration could be observed due to the higher kinetic energy of the spray droplets. The change in the air temperature from 50 to 150 °C leads to a slight increase in the penetration, which may be a result of the lower air density at higher temperatures under constant air pressure. The back pressure has the strongest impact on the spray length leading to a reduced penetration of the fuel jet. BF2 along with the Fischer-Tropsch fuel exhibit slightly shorter spray penetration in comparison to the reference fuel and BF1.

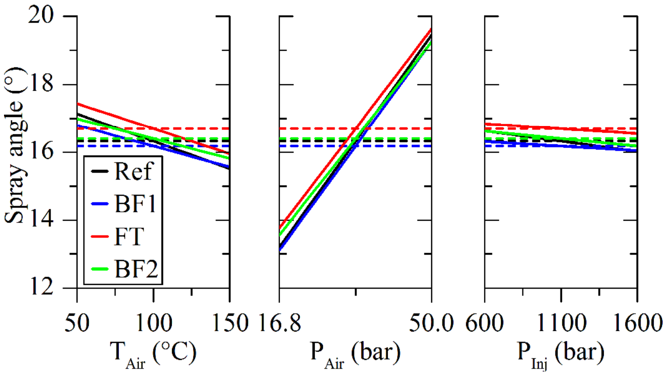

Figure 6 Effect of the operating parameters on the spray angle for all fuels

The higher spray momentum at higher injection pressures also helps the fuel droplets to overcome the air resistance resulting in a somewhat narrower spray angle, as shown in Figure 6. On the contrary an increase in the air pressure leads to wider spread of the fuel droplets thus wider spray angle, see Figure 6. At higher air temperature narrow spray angles can be observed due to evaporation at the spray edges or as a result of lower air density. Figure 6 clearly shows that the air pressure has the strongest impact on the cone angle whereas the dependence on the injection pressure is the smallest. Concerning the influence of the fuels wider spray angles were observed in the case of FT and BF2, which is in agreement with their shorter penetrations.

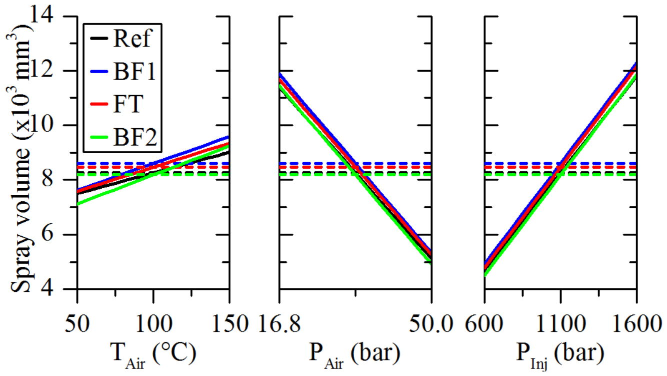

Figure 7 Effect of the operating parameters on spray volume for all fuels

Figure 7 shows the influence of the different parameters for the investigated fuels on the spay volume. The longer jet length leads to a larger spray volume with increasing injection pressure despite the slightly narrower spray angle, which indicates a better overall air entrainment, see Figure 7.The air resistance increases at higher air pressures, which leads to a more intense interaction of the fuel droplets interact with the air. This results in a reduction in the spray volume with increasing air density and therefore poorer air utilisation. Figure 7 depicts larger spray volume probably due to the lower air density. Slightly larger spray volume could be detected for BF1 and FT.

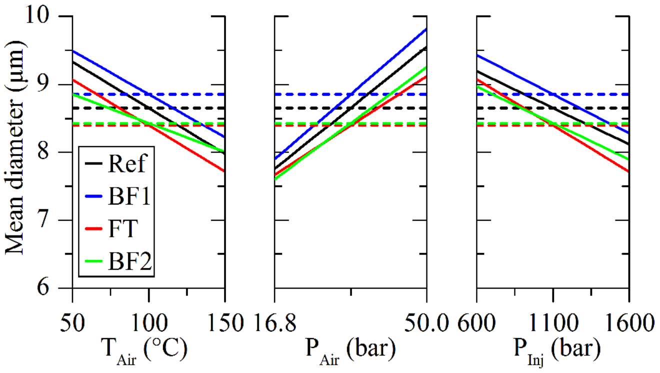

Figure 8 Effect of the operating parameters on the droplet mean diameter for all fuels

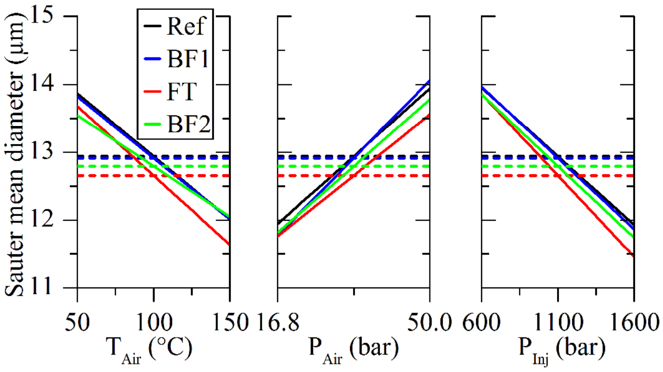

Figure 9 Effect of the operating parameters on the droplet SMD for all fuels

The increase of the injection pressure leads to a stronger spray breakup and thus a better atomisation, hence smaller mean and SMD, as it can be observed in Figure 8 and Figure 9. A higher air pressure should fundamentally enhance the air-drop interaction and thereby enhance the spray breakup. In dense sprays such as the diesel spray not only breakup mechanisms but also coalescence takes place, which may play an important role in this case as indicated by the larger droplets at higher air pressures, see Figure 8 and Figure 9. The increase of the air temperature promotes the droplet evaporation and thereby results in decrease of their diameters. All three parameters have strong impact on the droplet diameters, which is not the case for the spray geometry. The atomisation of the reference fuel and BF1 yields larger droplets meaning higher momentum, which corresponds to their longer penetration and narrower angle. FT and BF2 have smaller droplets, where the difference between them and the Diesel fuel and BF1 is larger in the case of the mean diameter, see Figure 8. This indicates that FT and BF2 have better atomisation in general with a relatively small amount of larger fuel droplets, which results in slightly increased SMD, which are comparable to those of the Diesel fuel. It is also noticeable that the change of the operating parameters has a stronger impact on the breakup of BF2 and FT leading to an increased difference between them.

OUTLOOK

The conducted investigations showed that the chosen second generation alternative Diesel fuels have similar atomisation and spray characteristics. Similar trend about the spray geometry of first and second generation alternative diesel fuels could be observed in previous investigations carried out in an optical engine [13]. This raises the question if their combustion behaviour and as result exhaust emissions are also alike. In order to investigate the soot formation and oxidation during the combustion of the fuels of interest a measurement campaign was started.

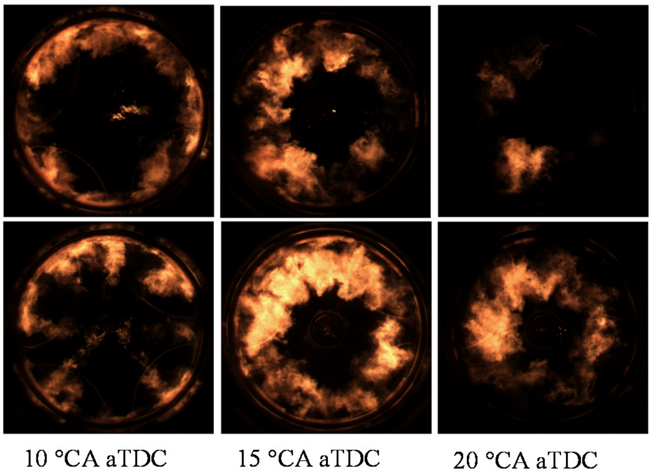

Figure 10 Soot luminosity of the reference fuel (top images) and BF2 (bottom images)

The preliminary result showed that the alternative fuels have a different combustion behaviour in comparison to conventional Diesel fuel. Figure 10 illustrates the natural soot luminosity of the reference fuel and BF2 at three crank angle positions. Larger soot clouds can be observed from the high speed imaging in the case of BF2, which may indicate an increased soot formation. Furthermore the intensity of the detected soot luminosity for the conventional Diesel fuel is lower than for BF2.

CONCLUSION

The aim of the current work was to analyse the spray characteristics of second generation alternative Diesel fuels. Therefore high speed visualisation techniques and phase Doppler anemometry were applied on a high pressure chamber in order to investigate the fuel atomisation and air-fuel mixing at engine like conditions. Additionally the influence of different ambient conditions on fuel atomisation and evaporation was investigated.

Generally speaking, only small differences could be detected between the investigated fuels due to the similarity of their physical properties. Still slightly wider spray angles could be observed in the case of BF2 and FT, whereas BF1 exhibited the smallest angles. At the same time smaller droplet diameters have been measured for BF2 and FT compared to the Diesel fuel. Moreover the mean and Sauter mean diameter of these two second generation fuels were strongly affected by the change of the operating parameters. BF1 showed the longest spray penetration and biggest mean diameter, suggesting a larger spray momentum.

The investigations showed that the alternative fuels have comparable air-fuel mixing properties to the Diesel fuel and the small difference in their spray characteristics could be accounted for by small changes in the operating conditions. Nevertheless the preliminary combustion analysis of the chosen fuels showed a strong influence of the fuel type on the combustion and exhaust emission formation processes, which cannot be explained by the atomisation analysis and physical properties of the fuels. This suggest that the chemical properties play a critical role in the combustion and therefore need to be thoroughly investigated in a future work.

ACKNOWLEDGEMENTS

The authors thank the federal state Sachsen-Anhalt financial support of this work in the Framework of the COMO project, the German Research Foundation in the frame work of the graduate school 1554 and the Institute of Automotive Expertise for providing the opportunity to work on their state-of-the-art single-cylinder test bed.

REFERENCES

1. Backofen, D., Tschöke, H., Könnig, M. Schmidt, J. *Extreme Hochdruckeinspritzung alternativer Dieselkraftstoffe - Von der Kraftstoffeinbringung bis zur Emissionsbildung*. in *Diesel- und Benzindirekteinspritzung*. 2012. Berlin: Haus der Technik.
2. Krome, D., *Characterisierung der Tropfenkollektive von Hochdruckeinspritzsystemen für direkteinspritzende Dieselmotoren*. 2004, Universität Hannover: Hannover.
3. Baert, R., Frijters, P., Somers, B., Luijten, C., de Boer, W., *Design and Operation of a High Pressure, High Temperature Cell for HD Diesel Spray Diagnostics: Guidelines and Results.* SAE Technical Paper, 2009-01-0649, 2009.
4. Blessing, M., *Untersuchung und Charakterisierung von Zerstäubung, Strahlausbreitung und Gemischbildung aktueller Dieseldirekteinspritzsysteme*, in *Institut für Verbrennungsmotoren und Kraftfahrwesen*. 2004, Universität Stuttgart: Stuttgart.
5. Hirleman, E.D., *History of Development of the Phase-Doppler Particle-Sizing Velocimeter.* Part. Part. Syst. Charact., 1996. 13: p. 59-67.
6. Lacoste, J., Crua, C., Heikal, M., Kennaird, D., Martin, G., *PDA Characterisation of Dense Diesel Sprays Using a Common-Rail Injection System.* SAE Technical Paper, 2003-01-3085, 2003.
7. Chen, P.-C., Wang, W.-C., Roberts, W. L., Fang, T., *Spray and Atomization of Diesel Fuel and its Alternatives from a Single-Hole Injector Using a Common Rail Fuel Injection System.* FUEL, 2013. 103: p. 850-861.
8. Ofner, B., *Phase Doppler Anemometry (PDA)*, in *Optical Measurements*, D.-I.O.F. Prof. em. Dr.-Ing. E.h. Franz Mayinger, Editor. 2001, Springer Berlin Heidelberg. p. 139-152.
9. Breuninger, T., *Untersuchung der Spraycharakteristik von Piezo-Injektoren in Bezug auf das Entflammungsverhalten beim strahlgeführten Brennverfahren*, in *Fakultät für Verfahrens- und Systemtechnik*. 2012, Otto-von-Guericke-Universität: Magdeburg.
10. Fischer, R.A., *The design of experiments*. Vol. 7. 1960, New York: Hafner.
11. Siebers, D., Higgins, B., Picket, L., *Flame Lift-Off on Direct-Injection Diesel Fuel Jets: Oxygen Concentration Effects.* SAE Technical Paper, 2002-01-0890, 2002.
12. Ranjit, K.R., *Design of Experiments Using the Taguchi Approach*. 2001, Hannover: John Wiley & Sons Inc.
13. Dragomirov, P., Sauerhering, J., Schmidt, J., Rottengruber, H., Hadler, J., Backofen, D. *Optical Analysis of High-pressure Injections in Transparent Engine*. in *European Conference on Liquid Atomization and Spray Systems*. 2013. Chaina, Greece: ILASS.